May 1998 • NREL/SR-520-24723

# Thin-Film Amorphous Silicon Alloy Research Partnership

## Final Technical Progress Report 2 February 1995–28 February 1998

S. Guha
*United Solar Systems Corporation*
*Troy, Michigan*


National Renewable Energy Laboratory
1617 Cole Boulevard
Golden, Colorado 80401-3393
A national laboratory of
the U.S. Department of Energy
Managed by Midwest Research Institute
for the U.S. Department of Energy
under Contract No. DE-AC36-83CH10093

NREL/SR-520-24723

# Thin-Film Amorphous Silicon Alloy Research Partnership

## Final Technical Progress Report
## 2 February 1995–28 February 1998

S. Guha
*United Solar Systems Corporation*
*Troy, Michigan*

NREL technical monitor: K. Zweibel


National Renewable Energy Laboratory
1617 Cole Boulevard
Golden, Colorado 80401-3393
A national laboratory of
the U.S. Department of Energy
Managed by Midwest Research Institute
for the U.S. Department of Energy
under Contract No. DE-AC36-83CH10093

Prepared under Subcontract No. ZAF-5-14142-01
May 1998

Available to DOE and DOE contractors from:
Office of Scientific and Technical Information (OSTI)
P.O. Box 62
Oak Ridge, TN 37831
Prices available by calling (423) 576-8401

Available to the public from:
National Technical Information Service (NTIS)
U.S. Department of Commerce
5285 Port Royal Road
Springfield, VA 22161
(703) 487-4650

# Preface

This Final Subcontract Report covers the work performed by United Solar Systems Corp. for the period 2 February 1995 to 28 February 1998 under DOE/NREL Subcontract No. ZAF-5-14142-01. The following personnel participated in the research program.

E. Akkashian, A. Banerjee, E. Chen, T. Glatfelter, S. Guha (Principal Investigator), M. Haag, G. Hammond, N. Jackett, M. Lycette, J. Noch, I. Rosenstein, D. Wolf, J. Yang, and K. Younan.

We would like to thank V. Trudeau for preparation of this report.

# Table of Contents

# List of Figures

# List of Tables

# Executive Summary

## Objectives

The principal objective of this R&D program is to expand, enhance and accelerate knowledge and capabilities for the development of high-performance, two-terminal multijunction amorphous silicon (a-Si) alloy modules. The near-term goal of the program is to achieve 12% stable module efficiency by 1998 using the multijunction approach.

## Approach

The major effort of the program is to develop high efficiency component and triple-junction cells with uniform property over large area so as to facilitate fabrication of monolithic modules of one-square-foot area. The component cells use materials of different bandgaps and incorporate Ge for the middle and the bottom cells. In order to reduce manufacturing cost by lowering material cost, improving throughput and minimizing optical and electrical losses associated with module fabrication, a novel laser-drilling approach has been developed and is being optimized. Investigations of long-term reliability of the modules through accelerated testing form an integral part of the program.

## Status/Accomplishments

- Investigations have been carried out on Ag/ZnO, Ag/$TiO_2$/ZnO and Ag/$MgF_2$/ZnO back reflectors to assess their suitability for use in cell structures. Incorporation of $TiO_2$ or $MgF_2$ is not found to give any additional advantage. Excellent uniformity has been achieved in the deposition of Ag/ZnO over one-square-foot area.

- Arrays of high efficiency component cells have been made over one-square-foot areas. Single-junction top cells have been made with an average stabilized power density of 5.4 mW/cm$^2$ measured under global AM1.5 illumination. Single-junction middle cells have been optimized to give average stabilized power density of 3.6 mW/cm$^2$ under global AM1.5 illumination with a cut-on filter with $\lambda > 530$ nm. Both these arrays are made on stainless steel substrate without any back reflector. Single-junction bottom cells have been fabricated on Ag/ZnO back reflectors with an average power density of 3.6 mW/cm$^2$ as measured under global AM1.5 illumination with a cut-on filter with $\lambda > 630$ nm.

- Arrays of high efficiency triple-junction cells of 0.25 cm$^2$ active-area have been fabricated over one-square-foot area with average stabilized efficiency of 12% as measured under AM1.5 illumination.

- A triple-junction module of aperture area 416 cm$^2$ has been fabricated with an initial efficiency of 11.7% and stabilized efficiency of 10.24%. A 922 cm$^2$ aperture-area module exhibited an initial efficiency of 11.5%.

- The novel laser-drilling approach has been used successfully to fabricate modules of one-square-foot area with shadow loss of approximately 1%.

- Using the novel laser-drilling approach, an initial total-area efficiency of 11.5% has been achieved in a triple-cell structure of 12.6 $cm^2$ area. An initial total-area efficiency of 10.6% has been achieved in a module of 300 $cm^2$ area.

- Reliability studies based on NREL's Interim Qualification Testing have been carried out to confirm the suitability of the module encapsulation materials and processes.

# Section 1

# Introduction

This report describes the research performed for a three-phase, three-year program under NREL Subcontract No. ZAF-5-14142-01. The research program is intended to expand, enhance and accelerate knowledge and capabilities for the development of high-performance, two-terminal multijunction amorphous silicon (a-Si) alloy modules.

It is now well recognized that a multijunction, multibandgap approach has the potential of achieving the highest stable efficiency in a-Si alloy solar cells. In this approach, the bandgap of the materials of the component cells is varied in order to capture a wide spectrum of the solar photons. Significant progress has been made in the development of materials and cell design in the last few years, and a stable module efficiency of 10.2% has been demonstrated over one-square-foot area using a triple-junction approach in which the bottom two component cells use amorphous silicon-germanium (a-SiGe) alloy. In order to meet the Department of Energy goal of achievement of 12% stable module efficiency by 1998, it is necessary to make further improvements in each of the component cells.

New back reflectors also need to be developed to facilitate improved light-trapping performance. Since the aim of the program is to develop a manufacturing technology, the research work must address issues involving scaleup, reliability and cost. It should be pointed out that reliability and cost issues encompass module interconnect and encapsulation methods as well.

The research report describes the activities carried out on various tasks that were taken up to address the above issues. In Section 2, we discuss investigations on back reflectors to improve cell performance, and investigate uniformity in performance over a one-square-foot area. In Section 3, we present results on performance of component cells, both in the initial and in the light-degraded states, deposited over a one-square-foot area. The uniformity in deposition is investigated by studying the performance of subcells deposited over the entire area. In Section 4, we present results on the performance of triple-junction cells and modules. The modules use grid-lines and encapsulants compatible with our production technology. In Section 5, we discuss the novel laser-processing technique that has been developed at United Solar to improve energy-conversion efficiency and reduce manufacturing cost. Detailed description of optimization of the processing steps and performance of laser-processed, triple-junction devices and modules are presented. Experimental results on investigations of reliability of modules are presented in Section 6. Future directions of the research work are outlined in Section 7.

# Section 2

# Back Reflector Study

## Introduction

One of the essential requirements in achieving high efficiency solar cells is that the back reflector must possess high reflectivity with light trapping quality. Our present textured Ag/ZnO back reflector has these properties and does give rise to significant enhancement in the red response. In our ongoing program, we have strived to further improve the Ag/ZnO back reflector property.

In this section, we present results of our study on specularity and uniformity of one-square foot, large-area Ag/ZnO back reflector. We shall also present the red response of the state-of-the-art a-SiGe alloy solar cells on Ag/ZnO. In addition, in order to study the effect of inserting a buffer layer in the back reflector stack, we have collaborated with Professor Roy Gordon of Harvard University. The results are also reported in this section.

## Specularity and Uniformity Study of Large-area Ag/ZnO Back Reflector

We have made an Ag/ZnO back reflector using the "RADLAS" machine. The deposition process consists of sequential deposition of Ag and ZnO films on a flexible large-area stainless steel substrate using a mangetron sputtering process. For uniformity studies on the back reflector, 2″ x 2″ sections are cut off and the integrated total reflectance measured as a function of wavelength. The specularity is measured in the red region using a wavelength characteristic of a He-Ne laser. Results on two different Ag/ZnO back reflectors are summarized below.

In the first example, Fig. 1 shows the reflectance in the wavelength range 800-950 nm at five different locations of a 900 $cm^2$ area Ag/ZnO back reflector. The values of reflectance at all the locations are in the range of 87-95 %. The specularity at the four corners and center are summarized in Table 1. The values range from 10.4-13.5%. The center of the back reflector usually has the highest specularity. Overall, as evaluated from Fig. 1 and Table 1, the uniformity in terms of both reflectance and specularity is good over the entire 900 $cm^2$ area.

**Table 1. Specularity Measurement at Various Locations on a 900 $cm^2$ Ag/ZnO Back Reflector.**

| Location | Specularity |
|---|---|
| NE corner | 10.4% |
| NW | 11.3% |
| SW | 11.5% |
| SE | 10.5% |
| Center | 13.5% |

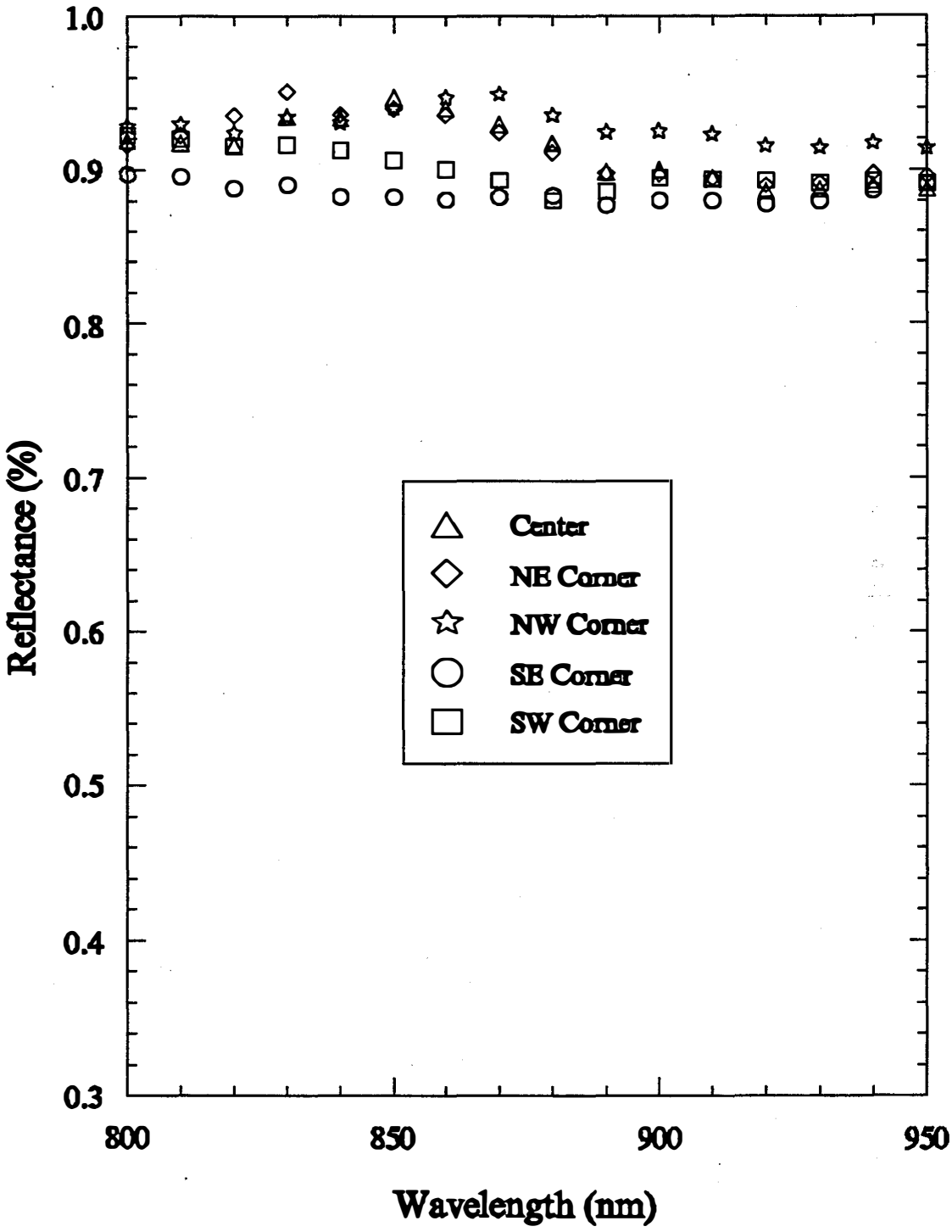


**Figure 1.** **Reflectance versus wavelength at several locations of a 900 $cm^2$ area Ag/ZnO back reflector.**

In the second example of Ag/ZnO back reflector R3351, the representative reflectance curve of a 2"x2" piece taken from the center of a one-square-foot back reflector is shown in Fig. 2. The total integrated reflectance in the wavelength range 800-950 nm is in the range of 77-87%. The specular component is 4%. Thus, the center piece satisfies the twin requirements of high reflectance and low specular component. The back reflector characteristics are expected to be similar over the entire area as determined from the uniformity studies shown in Fig. 1 and Table 1.

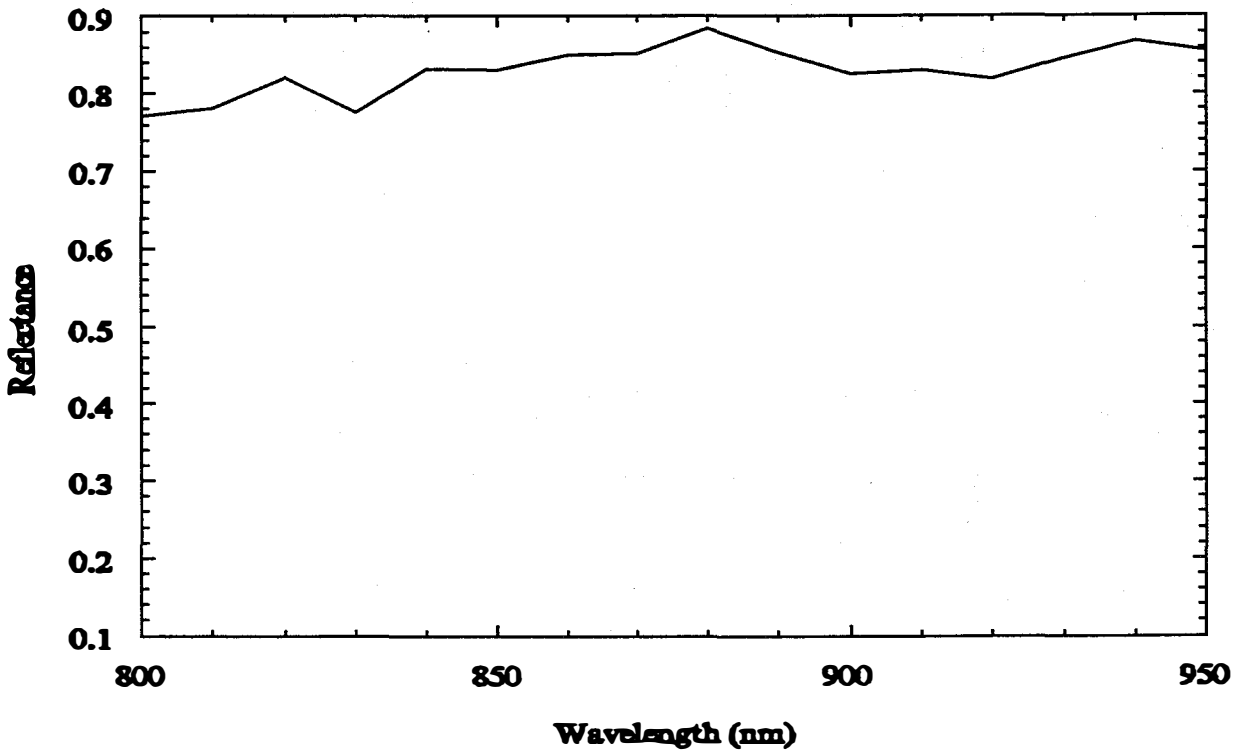


**Figure 2. Reflectance versus wavelength of Ag/ZnO back reflector R3351.**

Table 2 summarizes the results of the second case and the corresponding Phase III milestone for the back reflector. It shows that the values obtained exceed the milestone requirements of "the total integrated reflectance in the 800-950 nm range is greater than 85% with specular component less than 5%."

**Table 2. Summary of Ag/ZnO Back Reflector Characteristics and Phase II Milestones.**

| Back Reflector | Reflectance (800-950 nm) % | Specular Component (%) |
|---|---|---|
| R3351 Center | 77-87 | 4 |
| Phase III Milestone | > 85 | < 5 |

## Narrow Bandgap a-SiGe Alloy Solar Cells on Ag/ZnO with High Red Response

One of the methods to evaluate back reflectors is to deposit a narrow bandgap a-SiGe alloy solar cell and measure its quantum efficiency and evaluate its long-wavelength response. The best cell obtained to date measured under AM1.5 global illumination with a $\lambda$>630 nm cut-on filter has the following characteristics: $J_{sc}$ = 13.1 mA/cm$^2$, $V_{oc}$ = 0.622 V, FF = 0.635, and $P_{max}$ = 5.2 mW/cm$^2$. This represents the highest initial power achieved for an a-SiGe alloy cell. The quantum efficiency data versus wavelength data is shown in Fig. 3. The photocurrent evaluated from this Q curve is 25.8 mA/cm$^2$. At $\lambda$ = 850 nm, the quantum efficiency is 52%, reflecting the high quality of the back reflector.

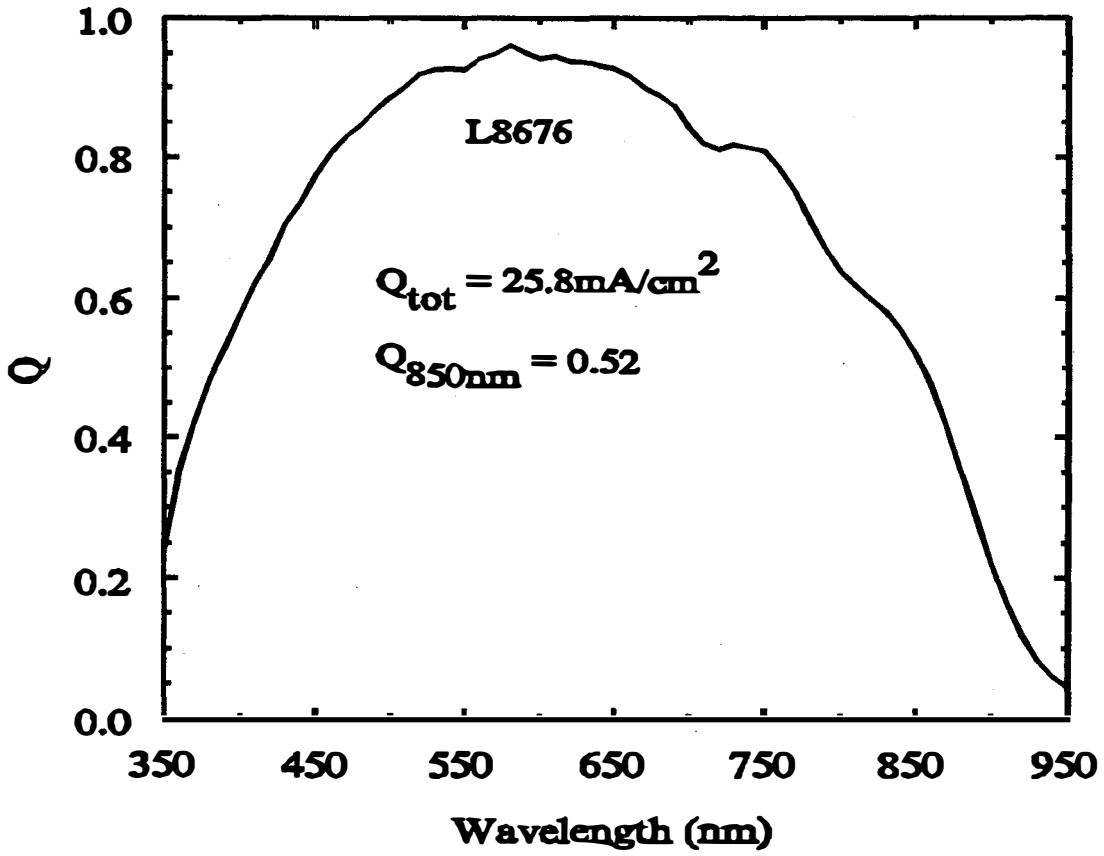


**Figure 3.** **Quantum efficiency versus wavelength for an a-SiGe alloy cell on Ag/ZnO back reflector.**

## Effect of Buffer Layer on Back Reflector Performance

One of the key factors which can improve the performance of a-Si alloy solar cell is the design of a suitable back reflector which will facilitate light trapping by total internal reflection. We have demonstrated significant increase in the short-circuit current density by the use of a textured Ag/ZnO back reflector. A careful analysis of the data, however, reveals that there may be parasitic losses associated with Ag/ZnO and/or ZnO/a-Si alloy interface. In order to study the effect of incorporating an additional buffer layer between ZnO and a-Si alloy, we have sent three ss/Ag/ZnO back reflectors to Prof. Roy Gordon of Harvard University for APCVD deposition of niobium doped titanium oxide. The motivation is to investigate if the titanium oxide layer would reduce parasitic loss and result in higher short-circuit current.

## Effect of Titanium Oxide Layer Between ZnO and a-Si Alloy

Figure 4 plots reflectivity measurements of four substrates versus wavelength. Substrate #1 is the control substrate which is our standard ss/Ag/ZnO back reflector, while substrates #2, #3, and #4 are standard ss/Ag/ZnO back reflectors coated with different thicknesses of titanium oxide. It should be pointed out that the reflectivity of titanium oxide coated back reflectors for samples #2 and #3 is higher than the control back reflector for long wavelengths.

We then proceeded to deposit narrow bandgap a-SiGe:H solar cells on these four substrates under identical conditions. Figure 5 plots the quantum efficiency and reflectivity curves versus wavelength for the four samples. It is observed that the control sample has the highest current for $\lambda$>630 nm. The additional titanium oxide layer apparently did not reduce any parasitic loss of the ZnO/a-Si alloy interface. Figure 6 plots the sum of quantum efficiency and reflectivity (Q+R) versus wavelength. The Q+R value turned out to be greater for the control sample for the long wavelength region indicating additional optical loss due to titanium oxide.

The J-V characteristics for $\lambda$>630 nm are summarized in Table 3. It should be pointed out that while we did not observe any enhancement in $J_{sc}$, the incorporation of the titanium oxide layer does not introduce any appreciable additional series resistance.

**Table 3. J-V Characteristics of a-SiGe:H *p i n* Solar Cells on Four Back Reflectors Measured under AM1.5 Illumination with a $\lambda$>630 nm Cut-on Filter.**

| Sample | Substrate | $J_{sc}$ (mA/cm$^2$) | $V_{oc}$ (V) | FF | $P_{max}$ (mW/cm$^2$) | $R_s$ ($\Omega$-cm$^2$) |
|---|---|---|---|---|---|---|
| 5008 | 1 | 8.72 | 0.678 | 0.535 | 3.16 | 24 |
| 5009 | 2 | 7.95 | 0.693 | 0.550 | 3.03 | 32 |
| 5012 | 3 | 8.10 | 0.678 | 0.512 | 2.81 | 30 |
| 5013 | 4 | 7.92 | 0.673 | 0.519 | 2.77 | 25 |

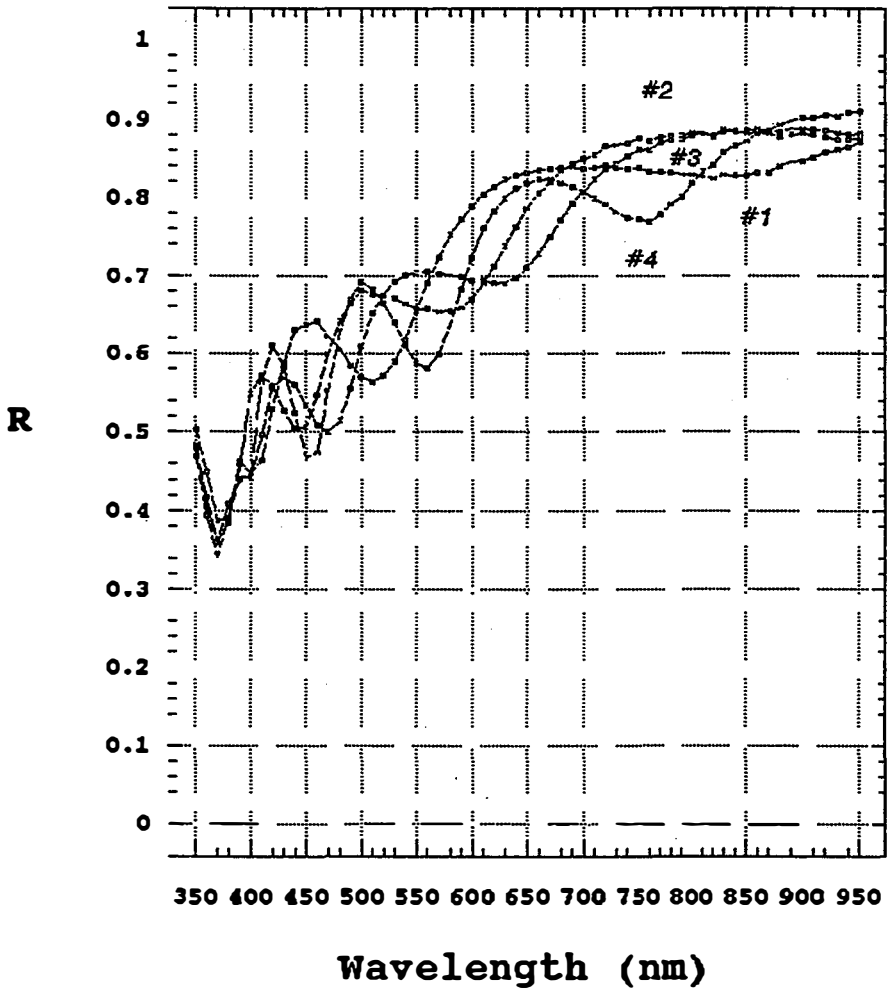


**Figure 4. Reflectivity versus wavelength for four substrates described in the text.**

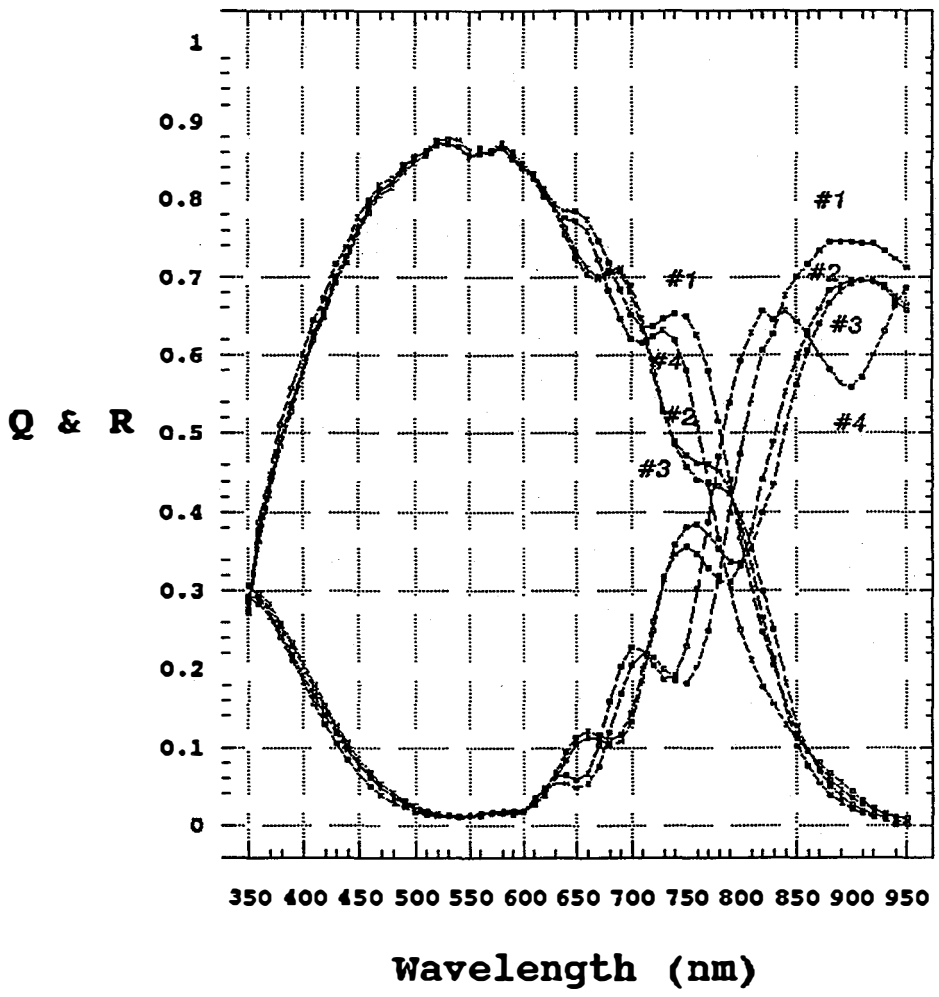


**Figure 5.** **Quantum efficiency and reflectivity curves versus wavelength for four a-SiGe:H solar cells on the four substrates in Fig. 4.**

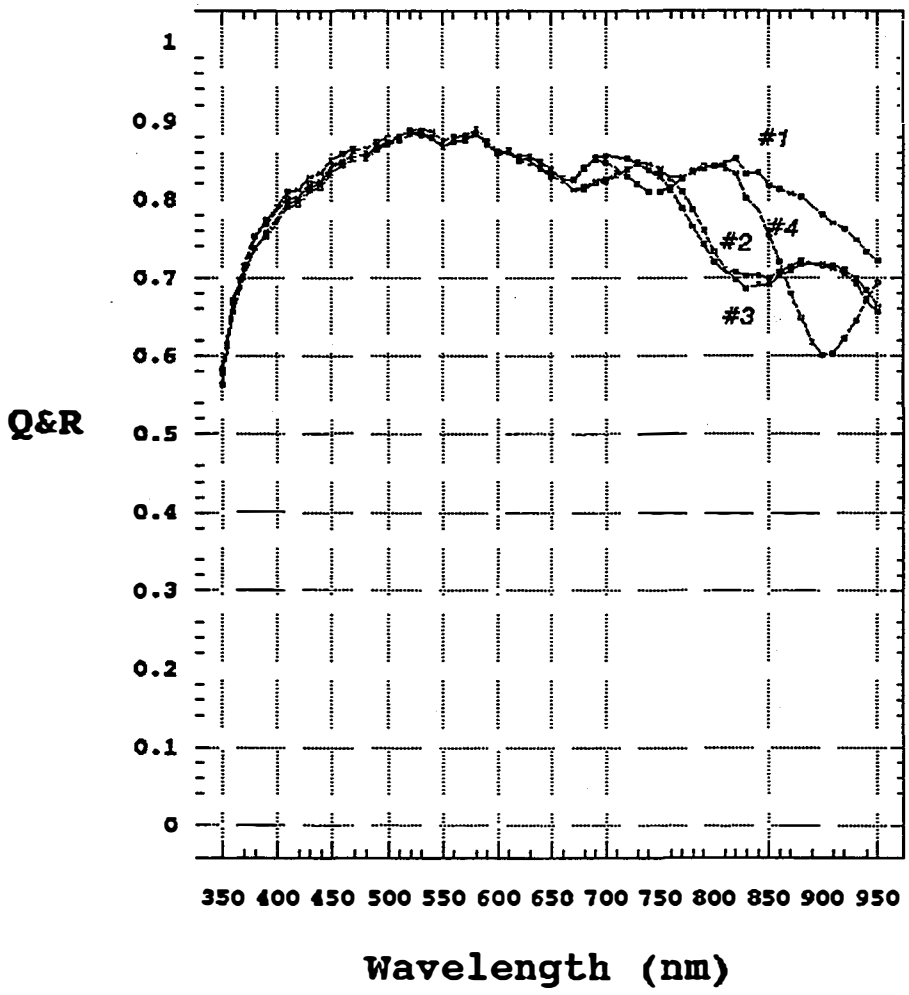


**Figure 6.** **Sum of quantum efficiency and reflectivity curves versus wavelength for the four samples in Fig. 5.**

## Effect of Magnesium Fluoride Layer Between Ag and ZnO

In addition, in our laboratory, we have developed an optically transparent magnesium fluoride ($MgF_2$). As it is a reasonably dense material, we expect that it would serve as an optical buffer layer. This proved to be the case as illustrated in Fig. 7. This figure displays the reflection dispersion for two structures: a stainless steel substrate coated with our standard BR materials of Ag and ZnO and the same structure but with $MgF_2$ deposited between the Ag and ZnO depositions. The $MgF_2$ was grown by thermal evaporation. The film is approximately 3000 Å thick. Notice in Fig. 7 that the effect of the inserted $MgF_2$ is to improve the reflection. It was our hope that the improvement was due to a repair of a parasitic optical loss at the Ag/ZnO interface. Therefore, we expected an improvement in the optical response of solar cells made on top of this new BR.

Unfortunately, $MgF_2$ is an electrical insulator. Thus, it is difficult to use as one of the layers in our standard solar cell structures. However, we devised a technique to make working solar cells with the $MgF_2$ layer as part of the structure. It involves "drilling" microscopic holes into the substrate immediately after the $MgF_2$ layer is deposited and prior to the ZnO coating. If the holes are appropriately dense, then the holes will conduct the solar cell current with only slight loss and lateral conduction may be provided by the ZnO layer. In our lab, we have a computer controlled apparatus consisting of a precision x-y positioner, an optical alignment system, and a Nb-YAG laser. This equipment was used to "drill" the required holes to provide to us a method of making solar cells using the enhanced structure as seen in Fig. 7.

Identical *n i p* devices of a-SiGe:H were deposited onto each of the substrates of Fig. 7. The spectral response of the cells were measured and integrated with respect to AM1.5 Standard Global Spectrum. The resulting current densities are presented in Table 4. We were disappointed to discover that the new $MgF_2$ did *not* result in any current enhancement. In this table we also display integrated currents for only wavelengths greater than 630 nm. This integration was performed to eliminate any differences in the spectral response curves due to factors other than the substrate effects. As seen in Table 4, this calculation is consistent with the overall integrated spectral response. Therefore, we must conclude that the $MgF_2$ did not give any optical enhancement. At present, we do not understand the reason for the reflection data of Fig. 7. We theorize that the interpretation of reflection spectra from textured surfaces where the size of the texture is of the order of the wavelength is not straight forward. We continue to believe that solar cells made using our standard structure are influenced by parasitic optical losses. However, we do not know the extent of the effect of the losses on the short circuit current of solar cells. The two-dimensional model developed by Bhushan Sopori of National Renewable Energy Laboratory may be able to shed further light on these issues.

**Table 4. Integrated Short-circuit Currents of the Structures Described in the Text.**

| Structure | Jsc-AM1.5 | Jsc->630nm |
|---|---|---|
| Ag/ZnO | 21.7 mA/cm$^2$ | 9.6 mA/cm$^2$ |
| Ag/$MgF_2$/ZnO | 21.2 mA/cm$^2$ | 9.2 mA/cm$^2$ |

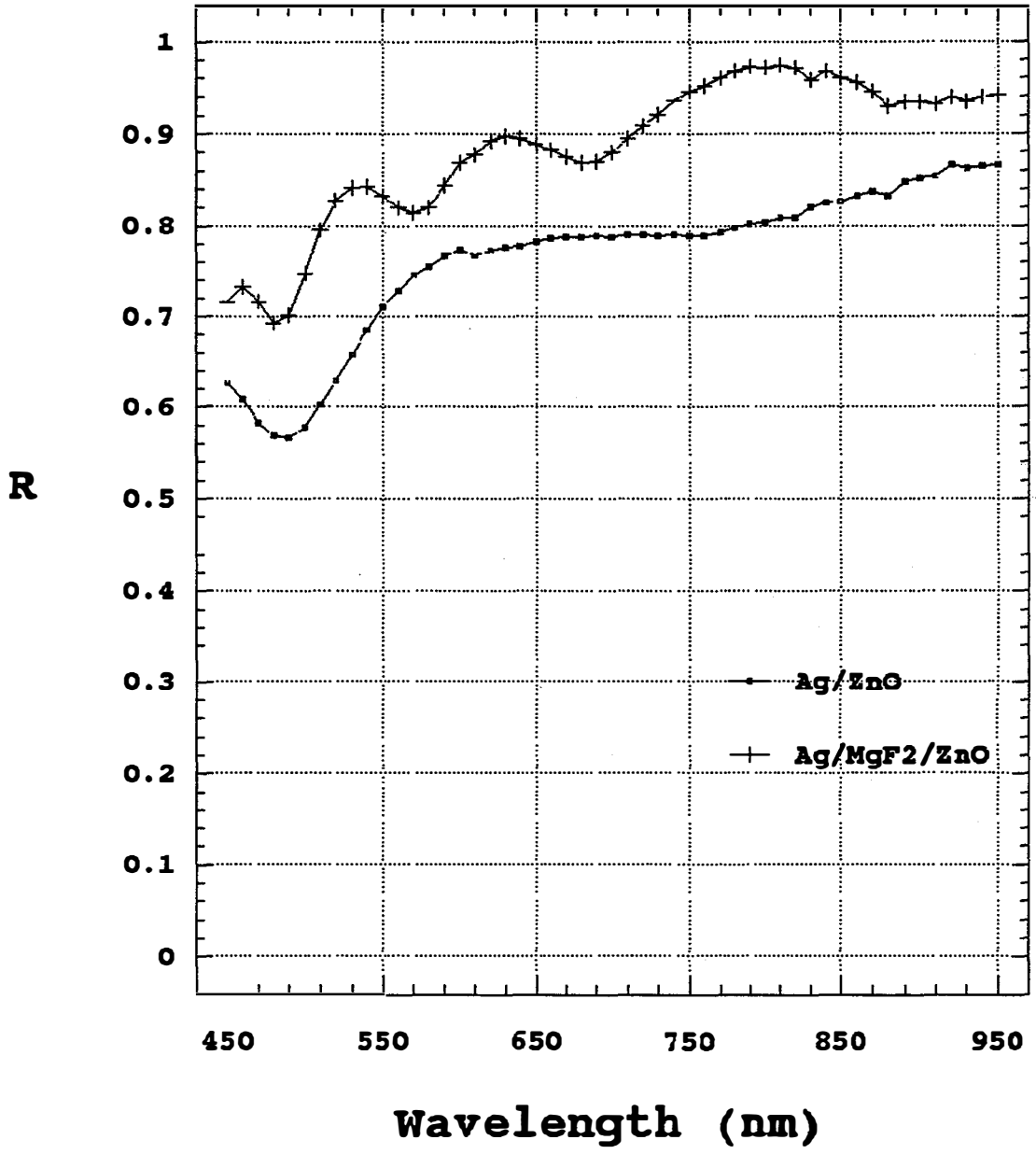


**Figure 7.** **Reflection versus wavelength of the incident light for two back reflector structures described in the text.**

# Section 3

# Status of a-Si Alloy and a-SiGe Alloy Component Cells

## Introduction

In order to obtain high efficiency multijuncton devices for module fabrication, two conditions have to be met. First, it is necessary to optimize the component top, middle, and bottom cells on appropriate substrates. Second, the uniformity of the component cell efficiency over the module area should be good. In this section both issues are addressed. All the results reported here have been obtained on devices made in the 2B machine. The 2B reactor is a multichamber rf glow discharge system capable of depositing amorphous silicon alloy layers over one-square-foot substrates.

## Device Fabrication and Measurement

The starting substrate material is a thin stainless steel (ss) sheet of approximately one-square-foot area. The back reflector (BR) consists of textured Ag/ZnO films deposited over the one-square-foot area by sputtering. The semiconductor devices are made by conventional glow discharge deposition over the entire area. The top transparent conducting oxide (TCO) layer is deposited in two different configurations. In the first, the TCO film covers the entire area. The TCO film is subsequently etched to yield an array of 11 x 12 (total of 132) devices each of active area 0.82 $cm^2$ (total area = 0.98 $cm^2$). The array covers an area of approximately 900 $cm^2$. I-V measurements are made on each device. The uniformity of device performance is evaluated by making contour plots for the one-square-foot area. In the second type of TCO, the substrate is cut into 2" x 2" pieces and TCO is deposited through an evaporation mask to yield devices of active area 0.25 $cm^2$ and 1 $cm^2$ area.

The top a-Si alloy cell is normally deposited on ss substrates with no back reflector and measured under AM1.5 condition. The rationale is that the top cell in the triple-junction configuration sees the full spectrum of the incident light but does not receive any reflected light since the underlying a-SiGe alloy cells starve it of any reflected light. It should be noted that the back reflector texture is known to have a deleterious effect on $V_{oc}$ and FF. Therefore, the correlation between the device performance on the stainless steel substrate and the simulated performance of the corresponding component cell in the triple-junction structure has some limitations.

For similar reasons as for the top cell, the middle component a-SiGe alloy cell consisting of intermediate bandgap a-SiGe alloy *i* layer is also deposited on ss substrate with no back reflector. In this case, the error in the simulation is slightly higher since the middle cell in the triple-junction configuration receives a small amount of reflected light. The I-V measurements on the middle cell are done through a bandpass filter of $\lambda > 530$ in order to simulate the filtering effect of the incident light of the top cell.

The bottom component cell using narrow bandgap a-SiGe alloy *i* layer is deposited on a textured Ag/ZnO back reflector. The I-V measurements are made through a bandpass filter of $\lambda > 630$ nm in order to simulate the light which the device receives in the triple-junction structure.

## Light Soaking

The component cells have been light-soaked to determine the stabilized values. The devices were degraded under one-sun, open-circuit, and 50 °C conditions for over 600 hours. The middle and bottom component cells were illuminated through appropriate high wavelength cut-on filters to simulate the short-circuit current density which the respective devices produce in the triple-junction configuration. The stabilized values of the top and middle cells on ss substrate and the bottom cell on BR are reported.

## Initial Results of a-Si Alloy Top Cell on ss

The top cell studies can be subdivided into two categories. In the first, we have explored the effect of deposition rate on cell performance. In the second, we have further optimized the deposition parameters of the low-rate material in order to achieve higher efficiency. The devices have been made in the small-area machines and the results are described below.

## Effect of Deposition Rate on Top Cell Performance

The effect of deposition rate on top cell performance is summarized below. We observed that as the deposition rate was increased from 2 Å/s to 3 Å/s, there was a decrease in $V_{oc}$ and FF. We have further studied the 3 Å/s deposition parameters and improved on the cell characteristics. Table 5 lists the initial J-V characteristics of a-Si alloy top cells with *i* layer deposited at 1, 2, 3 Å/s with the improved characteristics demonstrated in Sample #5779. The J-V characteristic for #5779 is shown in Fig. 8.

**Table 5. Initial J-V Characteristics of a-Si:H Top Cells on ss with Different Deposition Rates.**

| Sample | Deposition Rate (Å/s) | $J_{sc}$ (mA/cm$^2$) | $V_{oc}$ (V) | FF |
|---|---|---|---|---|
| Baseline | ~1 | 8.65 | 1.014 | 0.780 |
| 5635 | ~2 | 7.33 | 0.971 | 0.744 |
| 5691 | ~3 | 7.42 | 0.944 | 0.742 |
| 5779 | ~3 | 8.36 | 0.954 | 0.750 |

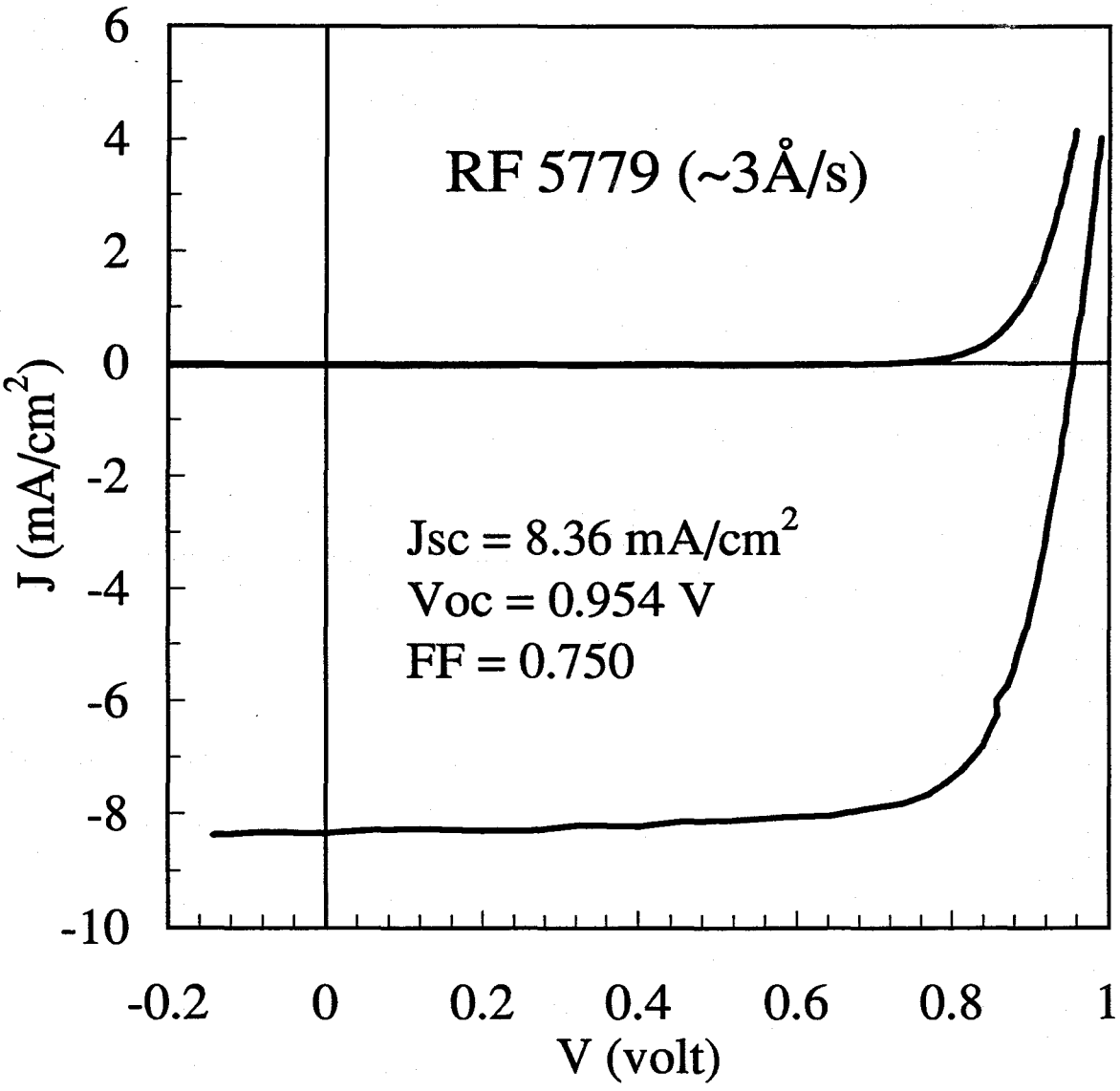


**Figure 8. J-V characteristics of an a-Si alloy cell with deposition rate of 3 Å/s.**

## Low Deposition Rate Top Cell

From our earlier studies in the design of a triple-junction structure, it is concluded that using the top cell as the current-limiting component cell is very desirable. The performance of the top cell, therefore, is very important. Optimization of cell parameters has led to further gains in device efficiency. The results of two improved devices are summarized in Table 6. The values of $V_{oc}$, FF, $J_{sc}$, and $P_{max}$ of device LINE 8675 are 1.011 V, 0.782, 8.68 mA/cm$^2$, and 6.86 mW/cm$^2$, respectively. These represent the highest values reported for an a-Si alloy cell of this structure. The J-V characteristics are shown in Fig. 9. The values of $V_{oc}$, FF, $J_{sc}$, and $P_{max}$ for LINE 8886 are 0.980 V, 0.761, 8.97 mA/cm$^2$, and 6.69 mW/cm$^2$, respectively. The result of two top cells on stainless steel substrate made in the 2B machine are also shown in Table 6. The values of $V_{oc}$, FF, $J_{sc}$, and $P_{max}$ of 2B 5178 are 0.998 V, 0.754, 8.6 mA/cm$^2$, and 6.46 mW/cm$^2$. The J-V characteristics of 2B 5178 are shown in Fig. 10. The values of $V_{oc}$, FF, $J_{sc}$, and $P_{max}$ of 2B 4568 are 1.014 V, 0.755, 8.09 mA/cm$^2$, and 6.19 mW/cm$^2$, respectively.

**Table 6. Initial Results of Top, Middle, and Bottom Component Cells of Area 0.25cm$^2$.**

| Type | Sample # | Substrate | Measurement Spectrum | $V_{oc}$ (V) | $J_{sc}$ (mA/cm$^2$) | FF | $P_{max}$ (mW/cm$^2$) |
|---|---|---|---|---|---|---|---|
| Top | L8675 | ss | AM1.5 | 1.011 | 8.68 | 0.782 | 6.86 |
| | L8886 | ss | AM1.5 | 0.980 | 8.97 | 0.761 | 6.69 |
| | 2B5178 | ss | AM1.5 | 0.998 | 8.60 | 0.754 | 6.46 |
| | 2B4568 | ss | AM1.5 | 1.014 | 8.09 | 0.755 | 6.19 |
| Middle | 2B4599 | ss | $\lambda$>530nm | 0.704 | 9.48 | 0.701 | 4.68 |
| | 2B4569 | ss | $\lambda$>530nm | 0.702 | 9.40 | 0.689 | 4.55 |
| Bottom | 2B5216 | Ag/ZnO | $\lambda$>630nm | 0.609 | 12.29 | 0.605 | 4.53 |
| | 2B4261 | Ag/ZnO | $\lambda$>630nm | 0.630 | 11.50 | 0.633 | 4.59 |

As mentioned above, the uniformity of the top cell performance on ss substrate has been evaluated by measuring the I-V characteristics of an array of 11 x 12 devices each of active area 0.82 cm$^2$. The contour plot of the normalized efficiency is shown in Fig. 11. The contour values range from 0.94 to 1.0, implying a uniformity of approximately 94% over the 900 cm$^2$ area.

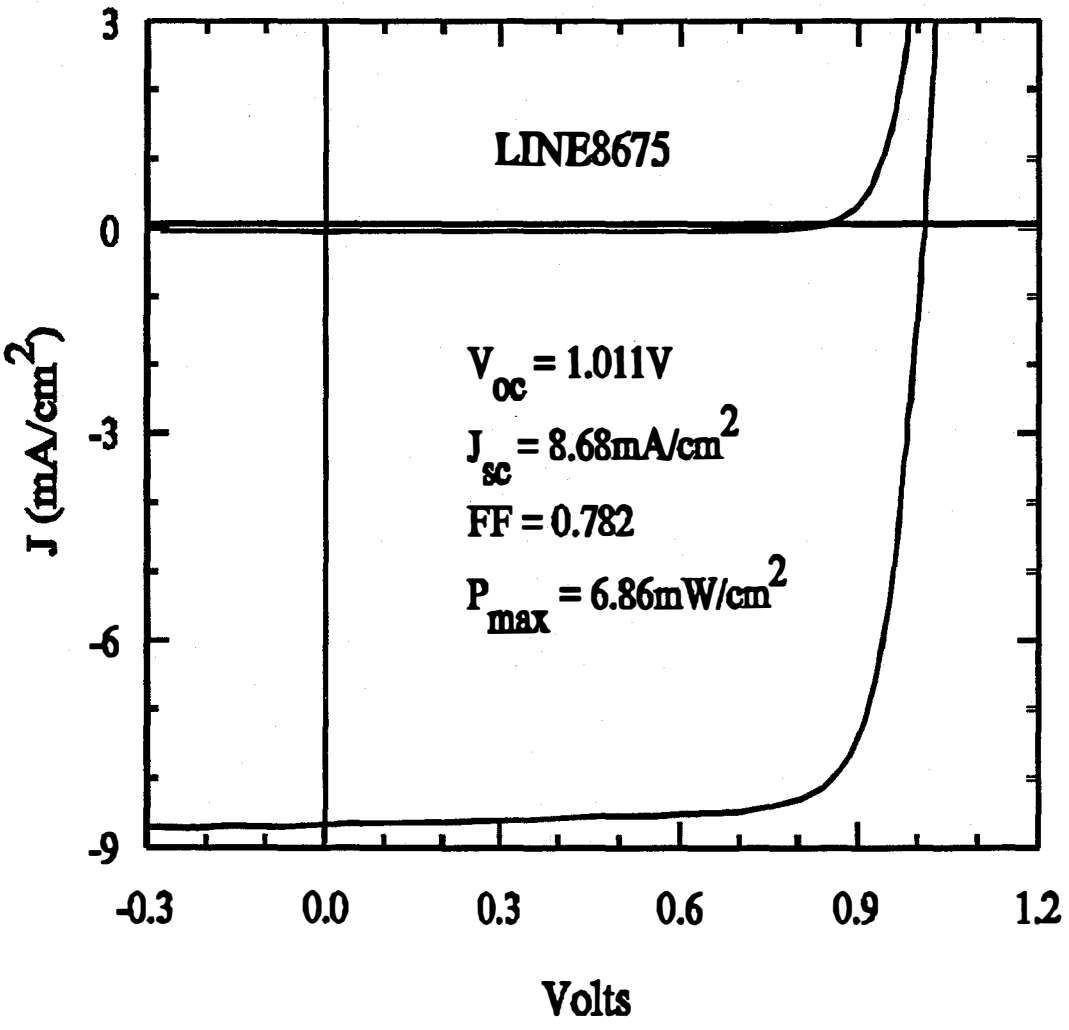


**Figure 9.** **Initial J-V characteristics of 0.25 cm$^2$ area a-Si alloy top cell LINE 8675 on stainless steel.**

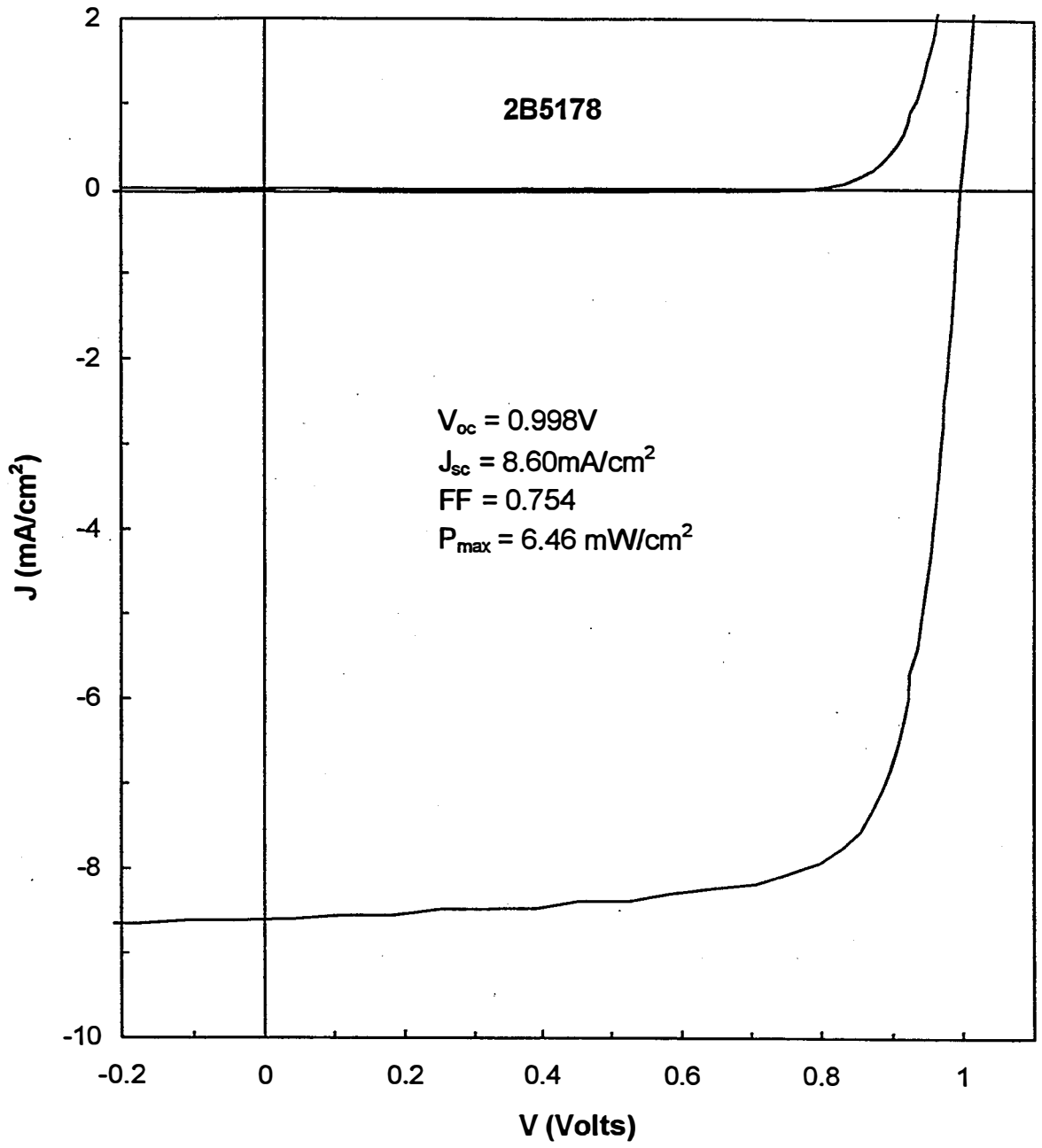


**Figure 10. Initial J-V characteristics of 0.25 cm$^2$ area top cell 2B5178 on ss substrate.**

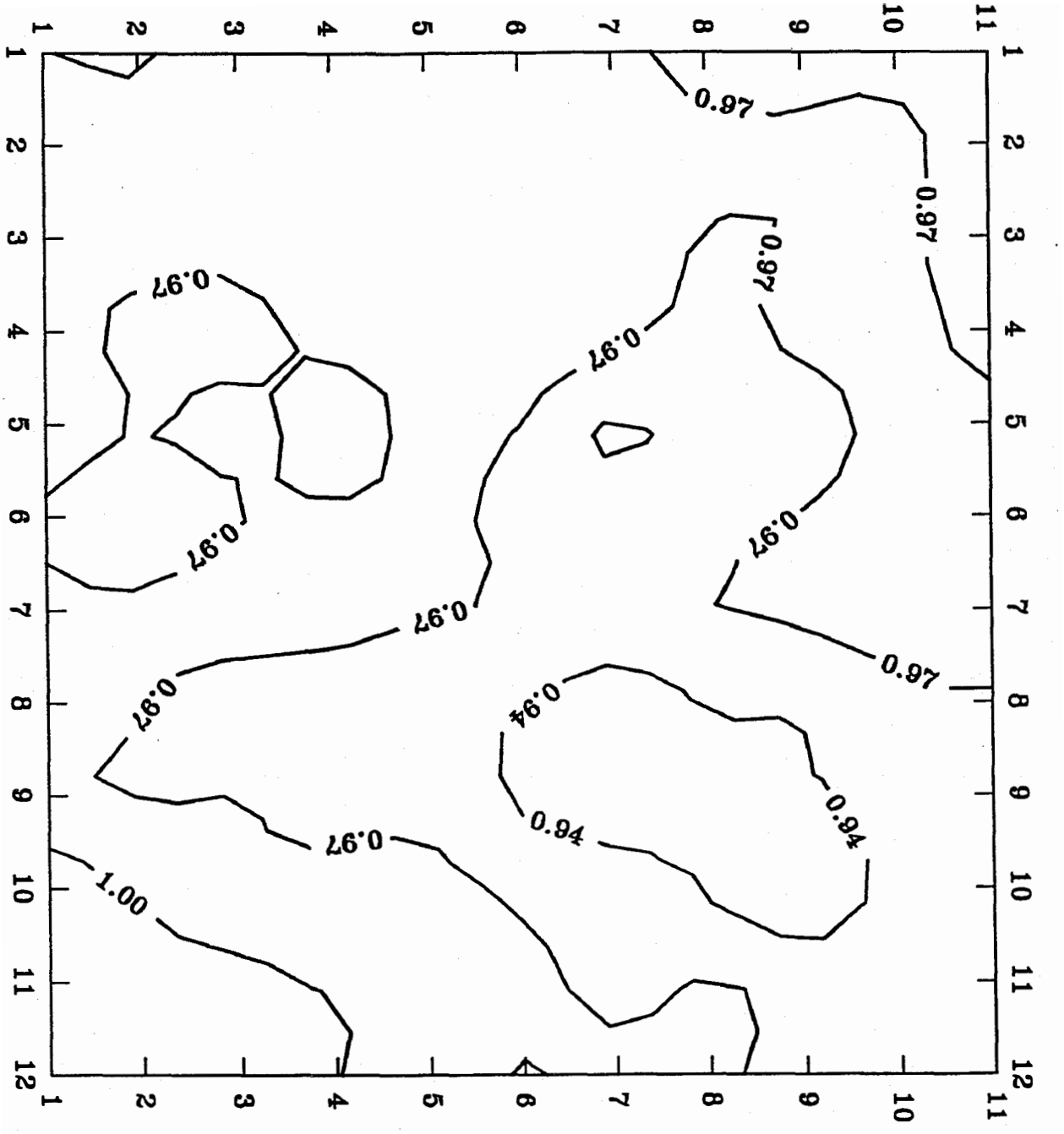


**Figure 11.** **Contour plot of normalized efficiency of the top cell on ss.** The figure represents a solar cell area of 900 $cm^2$.

## a-SiGe Alloy Middle Cell on ss

The initial results of two a-SiGe alloy middle cells on ss are summarized in Table 6. The device performance under AM1.5 illumination using $\lambda > 530$ nm cut-on filter is shown. The values of $V_{oc}$, $J_{sc}$, FF, and $P_{max}$ for the 2B 4599 with $\lambda > 530$ nm are 0.704 V, 9.48 mA/cm$^2$, 0.701 and 4.68 mW/cm$^2$, respectively. The J-V characteristics of the device is shown in Fig. 12. The corresponding values for 2B 4569 are 0.702 V, 9.40 mA/cm$^2$, 0.689, and 4.55 mW/cm$^2$, respectively. These good results are attributed to improvement in the material quality of the a-SiGe alloy incorporating more Ge than used before. The enhanced Ge content in the intrinsic layer results in extended red response without any significant deleterious effect on the current collection.

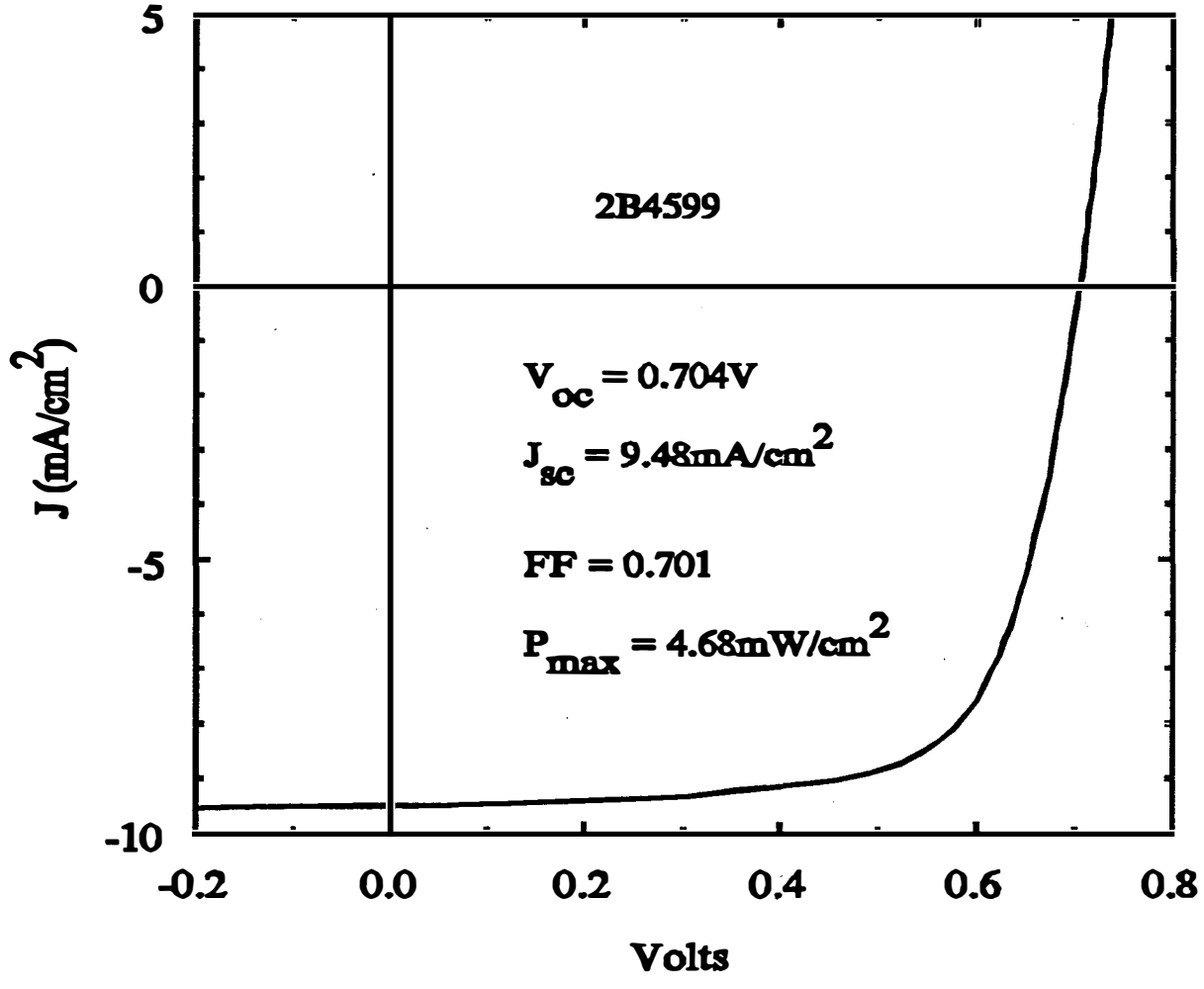


**Figure 12. Initial J-V characteristics of middle cell (>530nm) on ss substrate.**

The uniformity of the middle cell has been studied in a slightly different way than the top cell. Different sections of the 900 $cm^2$ device on the ss substrate were cut into ten representative 2" x 2" substrates. ITO dots of area 0.25 $cm^2$ and 1 $cm^2$ were deposited on the devices through an evaporation mask. The I-V characteristics were measured on all ten substrates. The spread in the average values of efficiency was within 5%, implying that the uniformity is within 5% over the entire area.

## a-SiGe Alloy Bottom Cell on Back Reflector

The initial performance of two bottom a-SiGe alloy narrow bandgap cells on Ag/ZnO BR are summarized in Table 6. The device performance under AM1.5 illumination using $\lambda > 630$ nm is given. The values of $V_{oc}$, FF, $J_{sc}$ (from Q measurements), and $P_{max}$ for 2B 5216 are 0.609 V, 0.605, 12.29 mA/$cm^2$ and 4.53 mW/$cm^2$, respectively. The I-V characteristics and Q curves of this device are shown in Fig. 13. The total $J_{sc}$ of the cell deduced from Q measurement is 26.00 mA/$cm^2$. The values of $V_{oc}$, FF, $J_{sc}$, and $P_{max}$ of the second device 2B 4261 are 0.630 V, 0.633, 11.50 mA/$cm^2$, and 4.59 mW/$cm^2$, respectively. These values represent significant gains in the achievement of high quality a-SiGe alloy of narrower bandgap than was possible in the past. The new device responds to even longer wavelength photons.

The uniformity of the bottom cell performance on BR substrate has been evaluated in a way similar to the top cell. The I-V characteristics of an array of 11 x 12 devices each of active area 0.82 $cm^2$ are measured. The contour plot of the normalized efficiency is shown in Fig. 14. The contour values range from 0.94 to 1.0, implying a uniformity of approximately 94% over the 900 $cm^2$ area.

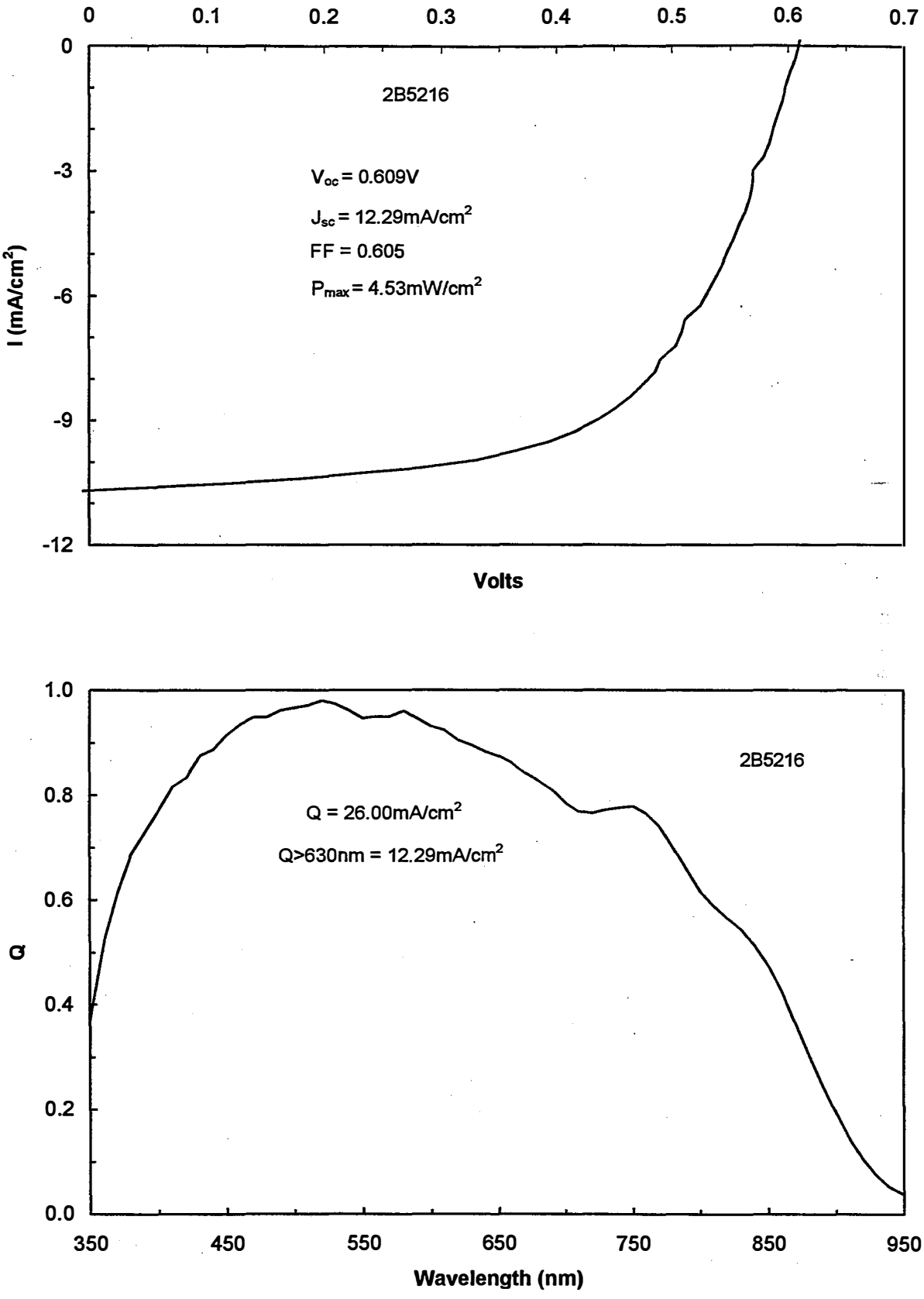


**Figure 13.** **Top: Initial I-V characteristics (>630 nm filter) and bottom: Q curve of bottom component cell.**

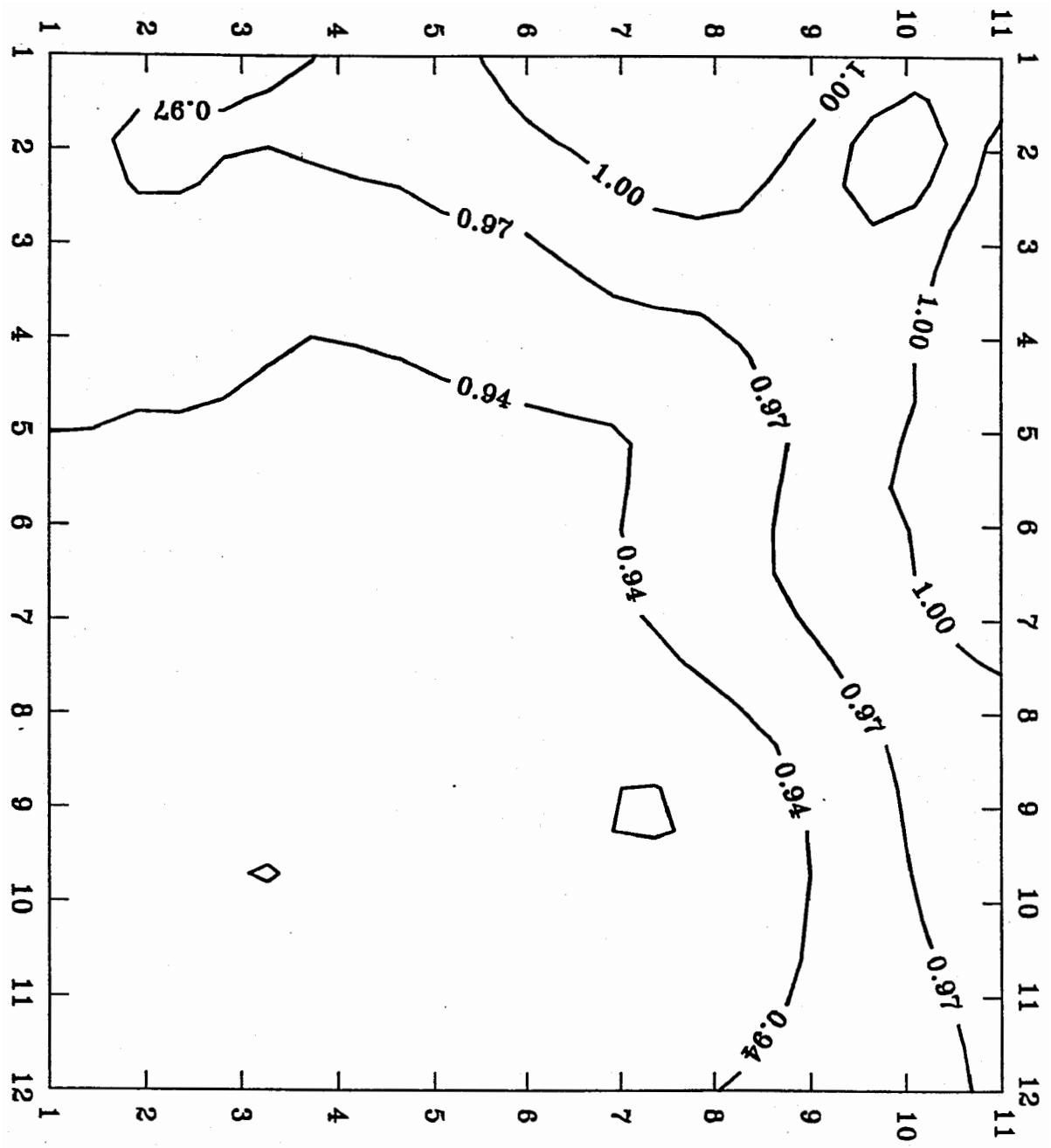


**Figure 14.** **Contour plot of normalized efficiency of the bottom cell on BR.** The figure represents an area of 900 $cm^2$.

## Stabilized Results of the Component Cells

The stabilized results of the top, middle, and bottom component cells are summarized in Table 7. For the purpose of comparison, the corresponding Phase III milestones are also tabulated. It may be noted that the best devices (highest initial efficiency) have not been subjected to light-soaking. The initial performance ($P_{max}$ only) of the best devices (taken from Table 6) are also shown in the table. Comparison of the initial values of $P_{max}$ of the best devices with those that have actually been light-soaked demonstrates that the stabilized efficiency of the best devices is expected to be higher than that being reported for all the categories.

**Table 7. Stabilized Results of the Top, Middle, and Bottom Component Cells.**

| Sample # | Area ($cm^2$) | Measurement Spectrum | $V_{oc}$ (V) | FF | $J_{sc}$ ($mA/cm^2$) | $P_{max}$ ($mW/cm^2$) | |
|---|---|---|---|---|---|---|---|
| | | | | | | Stable | Initial |
| **Top cell on ss** | | | | | | | |
| L8886 | 0.25 | AM1.5 | 0.953 | 0.709 | 8.78 | 5.9 | 6.7 |
| 2B4611 | 0.25 | AM1.5 | 0.962 | 0.692 | 8.2 | 5.4 | 6.4 |
| 2B4598 | 0.25 | AM1.5 | 0.960 | 0.686 | 8.2 | 5.4 | 6.4 |
| 2B5178 | 0.25 | AM1.5 | | | | | 6.5 |
| *Phase III Goal* | 1 | AM1.5 | 0.94 | 0.71 | 8.1 | 5.4 | |
| **Middle cell on ss** | | | | | | | |
| 2B4615 | 0.25 | λ>530nm | 0.654 | 0.576 | 9.3 | 3.5 | 4.5 |
| 2B4599 | 0.25 | λ>530nm | 0.665 | 0.576 | 9.3 | 3.6 | 4.6 |
| *Phase III Goal* | 1 | λ>530nm | 0.74 | 0.62 | 8.1 | 3.7 | |
| **Bottom cell on BR** | | | | | | | |
| 2B2484 | 0.82 | λ>630nm | 0.64 | 0.57 | 9.9 | 3.6 | 4.3 |
| 2B4261 | 0.25 | λ>630nm | | | | | 4.6 |
| *Phase III Goal* | 1 | λ>630nm | 0.66 | 0.61 | 8.4 | 3.4 | |

The stabilized results of three top cells--one from the LINE machine and two from the 2B machine--are shown in Table 7. Samples L8886, 2B 4611, and 2B 4598 were deposited directly on stainless steel. The AM1.5 results of LINE 8886 are $V_{oc}$ = 0.953 V, FF = 0.709, $J_{sc}$ = 8.78 mA/cm$^2$, and $P_{max}$ = 5.9 mW/cm$^2$. The stabilized 2B results for both the devices are $V_{oc}$ = 0.96 V, FF = 0.69, $J_{sc}$ = 8.2 mA/cm$^2$, and $P_{max}$ = 5.4 mW/cm$^2$. The Phase III goal is $V_{oc}$ = 0.94 V, FF = 0.71, $J_{sc}$ = 8.1 mA/cm$^2$, and $P_{max}$ = 5.4 mW/cm$^2$. Thus, the top cell results meet the milestone requirement. The initial $P_{max}$ of 6.5 mW/cm$^2$ for the best device 2B 5178 is higher than that of 2B 4611 or 2B 4598. The stabilized result of 2B 5178 is expected to be higher.

The stabilized results of two middle cells 2B 4615 and 2B 4599 on stainless steel are summarized in Table 7. The I-V characteristics were measured under AM1.5 illumination using a 530 nm cut-on filter. The cell parameters are $V_{oc}$ = 0.65-0.66 V, FF = 0.58, $J_{sc}$ = 9.3 mA/cm$^2$, and $P_{max}$ = 3.5-3.6 mW/cm$^2$. The Phase III goal is $V_{oc}$ = 0.74 V, FF = 0.62, $J_{sc}$ = 8.1 mA/cm$^2$, and $P_{max}$ = 3.7 mW/cm$^2$. Thus, the middle cell results are close to the requirement of the milestone.

The stabilized results of the bottom cell 2B 2484 on Ag/ZnO back reflector are summarized in Table 7. The measurements were made under AM1.5 illumination using a 630 nm cut-on filter. The device performance is $V_{oc}$ = 0.64 V, FF = 0.57, $J_{sc}$ = 9.9 mA/cm$^2$, and $P_{max}$ = 3.6 mW/cm$^2$. The Phase III goal is $V_{oc}$ = 0.66 V, FF = 0.61, $J_{sc}$ = 8.4 mA/cm$^2$, and $P_{max}$ = 3.4 mW/cm$^2$. Therefore, the bottom cell satisfies the milestone requirement. The best device 2B 4261 has an initial $P_{max}$ of 4.6 mW/cm$^2$ which is higher than that of 2B 2484. The stabilized result of 2B 4261 is expected to be better than that of 2B 2484.

# Section 4

# Status of Triple-Junction Solar Cells and Modules

## Introduction

Triple-junction triple-bandgap approach has been adopted to obtain high efficiency multijunction devices. The bottom and middle cells employ narrow bandgap and intermediate bandgap a-SiGe alloy *i* layers, respectively. The top cell uses a-Si alloy *i* layer. The status of the initial efficiency and stabilized efficiency of the component cells have been described in Section 3. In this section, the status of the triple-junction devices and modules is described. An initial module efficiency of 11.7% has been obtained.

## Triple-junction Solar Cells

The triple-junction devices have been made in the 2B machine using a procedure similar to the one used for component cells as described in Section 3. Representative 2" x 2" substrates have been cut out for evaluation. All the devices have been fabricated on Ag/ZnO BR and the active area of the devices is 0.25 $cm^2$. For best performance, the device should be top-cell current limited. The current contributions from the top, middle, and bottom cells have been obtained from Q versus wavelength measurements. The current density of the limiting cell has been used as the short-circuit current density of the device. The stabilized values have been obtained after more than 1000 hours of one-sun illumination under 50 °C and open-circuit conditions.

Table 8 summarizes the initial and stabilized results of triple-junction devices measured under AM1.5 conditions. The performance of sample 2B 4740 is $V_{oc}$ = 2.244 V, $J_{sc}$ = 8.54 mA/$cm^2$, FF = 0.713, and efficiency = 13.66%. The current density contributions, as determined from quantum efficiency measurements, from the top, middle, and bottom cells are 8.88, 8.54, and 8.66 mA/$cm^2$. The current density of the limiting cell, $Q_{middle}$ = 8.54 mA/$cm^2$, is used as the current density of the device. Sample 2B 4374 exhibits an efficiency of 13.52%. The values of $V_{oc}$, $J_{sc}$, and FF are 2.291 V, 8.37 mA/$cm^2$, and 0.705, respectively. The current-density contributions of the top, middle, and bottom cells are 8.51, 8.48, and 8.37 mA/$cm^2$. The J-V characteristics and Q curves of 2B 4740 are shown in Fig. 15. Note that in the J-V characteristics, we have used the limiting cell current density as the $J_{sc}$ value. The stabilized results of sample 2B 4740 are summarized in Table 8. The stable efficiency of 2B 4740 is 11.99% which is slightly lower than the Phase III milestone of 12.30%.

**Table 8. Initial and Stabilized Results of 0.25$cm^2$ Area Triple-Junction Devices made on Ag/ZnO BR.**

| Sample # | Status | Voc (V) | Jsc (mA/$cm^2$) Top/Middle/Bottom (mA/$cm^2$) | FF | Efficiency (%) |
|---|---|---|---|---|---|
| 2B4740 | Initial | 2.244 | 8.54<br>8.88/8.54/8.66 | 0.713 | 13.66 |
| 2B4374 | Initial | 2.291 | 8.37<br>8.51/8.48/8.37 | 0.705 | 13.52 |
| 2B4740 | Stable | 2.176 | 8.52 | 0.648 | 11.99 |
| *Phase III Goal* | Stable | | | | 12.30 |

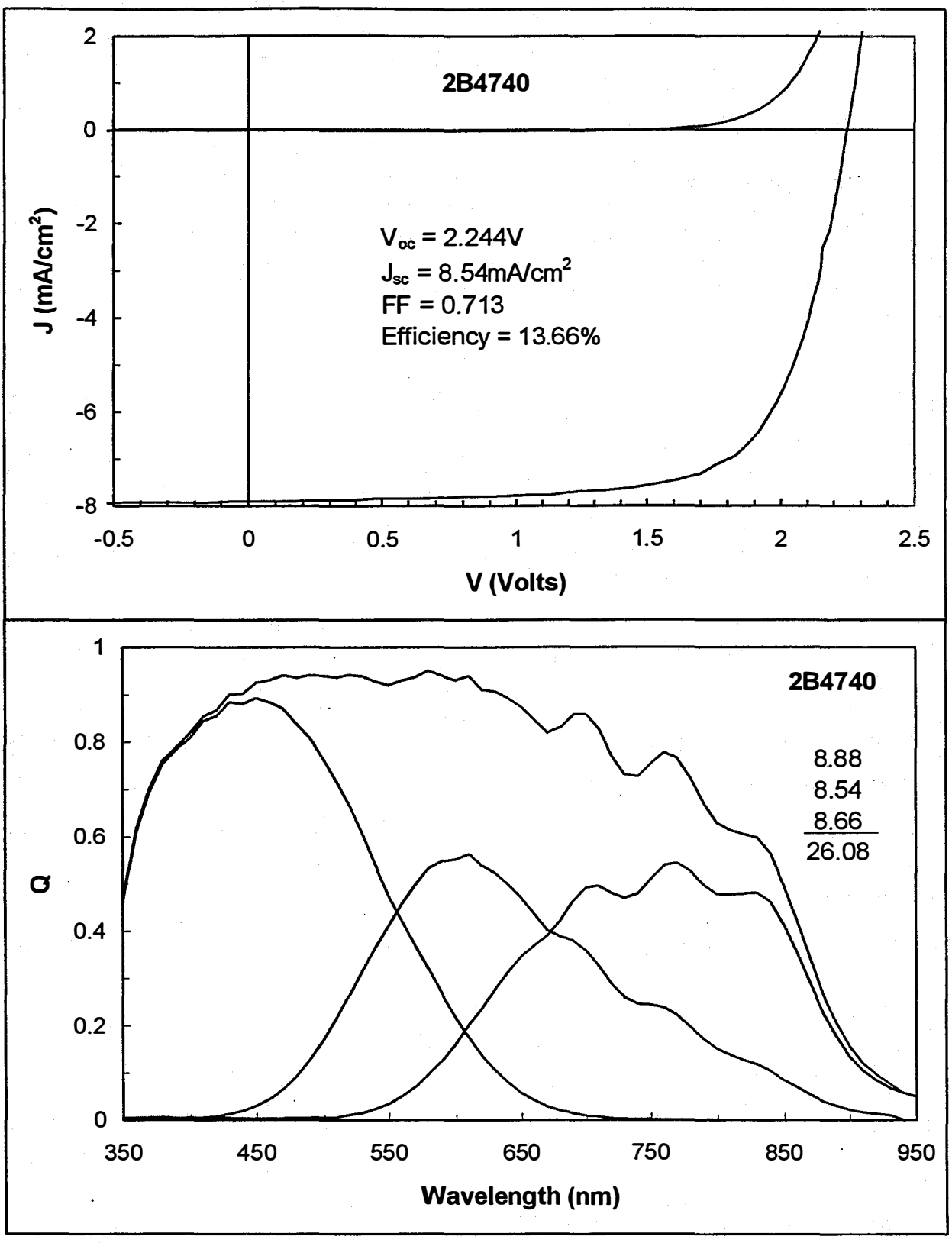


**Figure 15.** **J-V characteristics and Q curves of triple-junction device with initial efficiency of 13.66%.**

In order to ensure that the entire 900 $cm^2$ area satisfies the milestone values, the initial efficiency of all the 11 x 12 devices distributed over the 900 $cm^2$ were measured. The efficiency contour plot shown in Fig. 16 shows that the initial performance of the devices over the 900 $cm^2$ is quite uniform. The normalized contour values of 0.96 to 1.0 demonstrate that the uniformity is approximately 96% over the entire area.

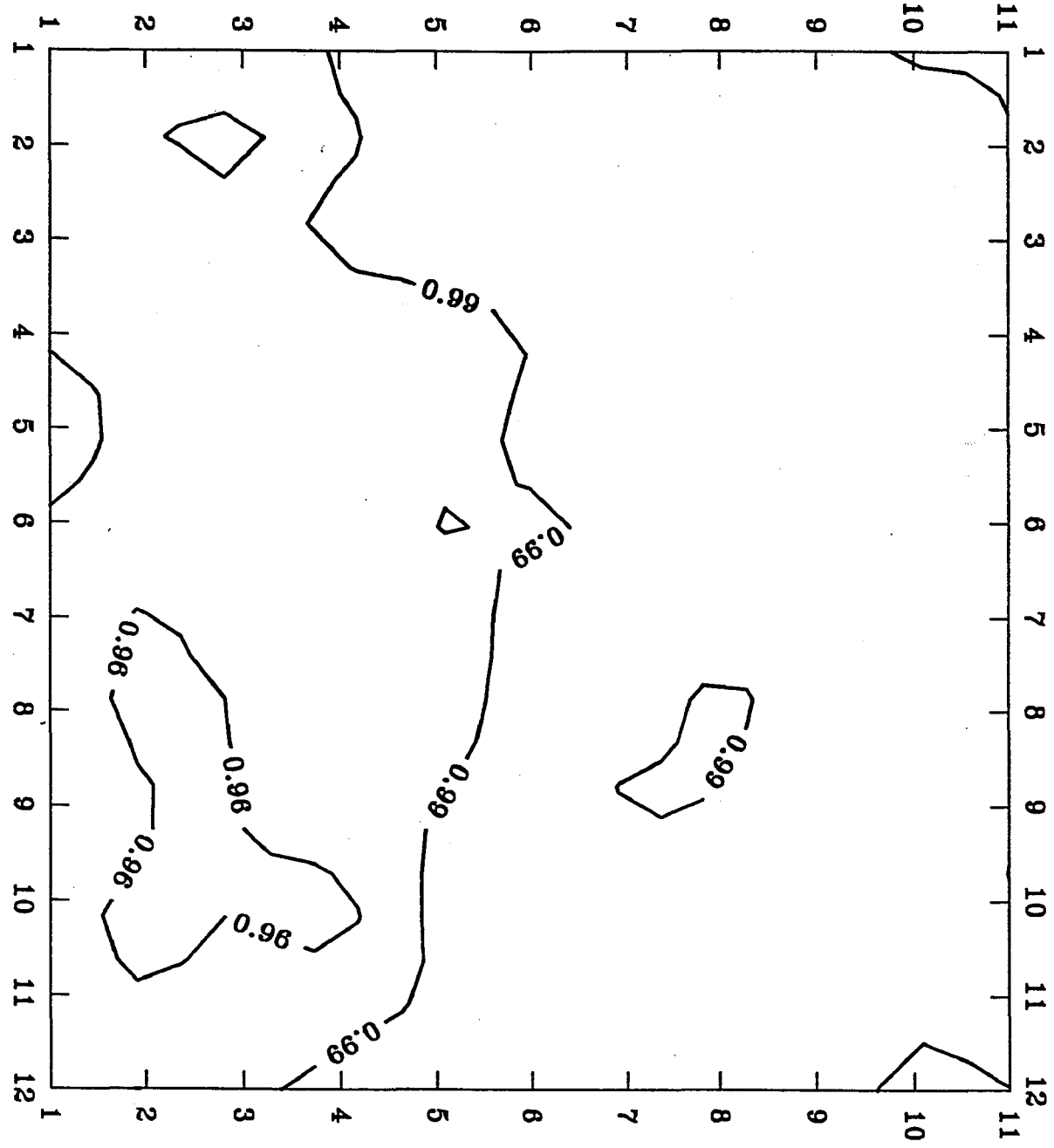


**Figure 16.** **Contour plot of normalized efficiency of the triple-junction cell.** The figure represents an area of 900 $cm^2$.

## Triple-junction Modules

### *Initial Results*

Extensive work has been done on developing a ~900 $cm^2$ aperture-area module which would pass the Interim Qualification Test Standard NREL/TR-213-3624 and also be production compatible. The primary focus of modules fabricated in the past was to obtain high stabilized efficiency, and there was no emphasis on qualification testing or production compatibility. The new design addresses both these important issues. The module design, assembly processes, structure, and materials used are similar to those being used in manufacturing. The new module design has come at a cost—the module optical losses are higher. Consequently, the module efficiency is lower even with the same or even slightly improved small-area device efficiency. Thus, any comparison of present module efficiency with that in the past must be done with some care.

The module design consists of a triple-junction device deposited on a stainless steel substrate with Ag/ZnO back reflector. The current is collected from the top using grid wires and bus bars. The device is encapsulated using EVA and Tefzel. Modules of different aperture areas have been fabricated.

Table 9 summarizes the initial results of six modules of different area. The last column gives the efficiency before encapsulation. The aperture area of modules 4661, 4674, and 4675 is 415-416 $cm^2$. Modules 472013, 473219, and 476239 have an aperture area of 920-922 $cm^2$. The efficiency of the smaller area modules is higher, 11.4-11.7%, compared to the larger ones, 11.2-11.5%. The efficiency of module 4675 is the highest, 11.7%. For module 4675, $V_{oc}$ = 2.29 V, $I_{sc}$ = 3.09 A, and FF = 0.690. The I-V characteristics of the module are shown in Fig. 17. Amongst the larger area modules, 473219 exhibits the highest efficiency, 11.5%. For module 473219, the aperture area = 922 $cm^2$, $V_{oc}$ = 4.51 V, $I_{sc}$ = 3.44 A, and FF = 0.684. The efficiency of the modules before encapsulation is usually higher because there is no reflection/absorption loss from the overlying encapsulant. The efficiency of the unencapsulated module 4674 is as high as 12.1%.

## Stabilized Results

Two of the modules from Table 9, 4661 and 4675, were light soaked under one-sun, open-circuit, and 50 °C conditions over 1000 hours. The stabilized results are summarized in Table 10. The stabilized values of efficiency are 10.10 and 10.24%. The Phase III milestone is 11.5%. Though the achieved results are lower than the milestone number, it should be noted that the new numbers represent an improvement over corresponding numbers reported previously since the new modules incorporate higher optical losses.

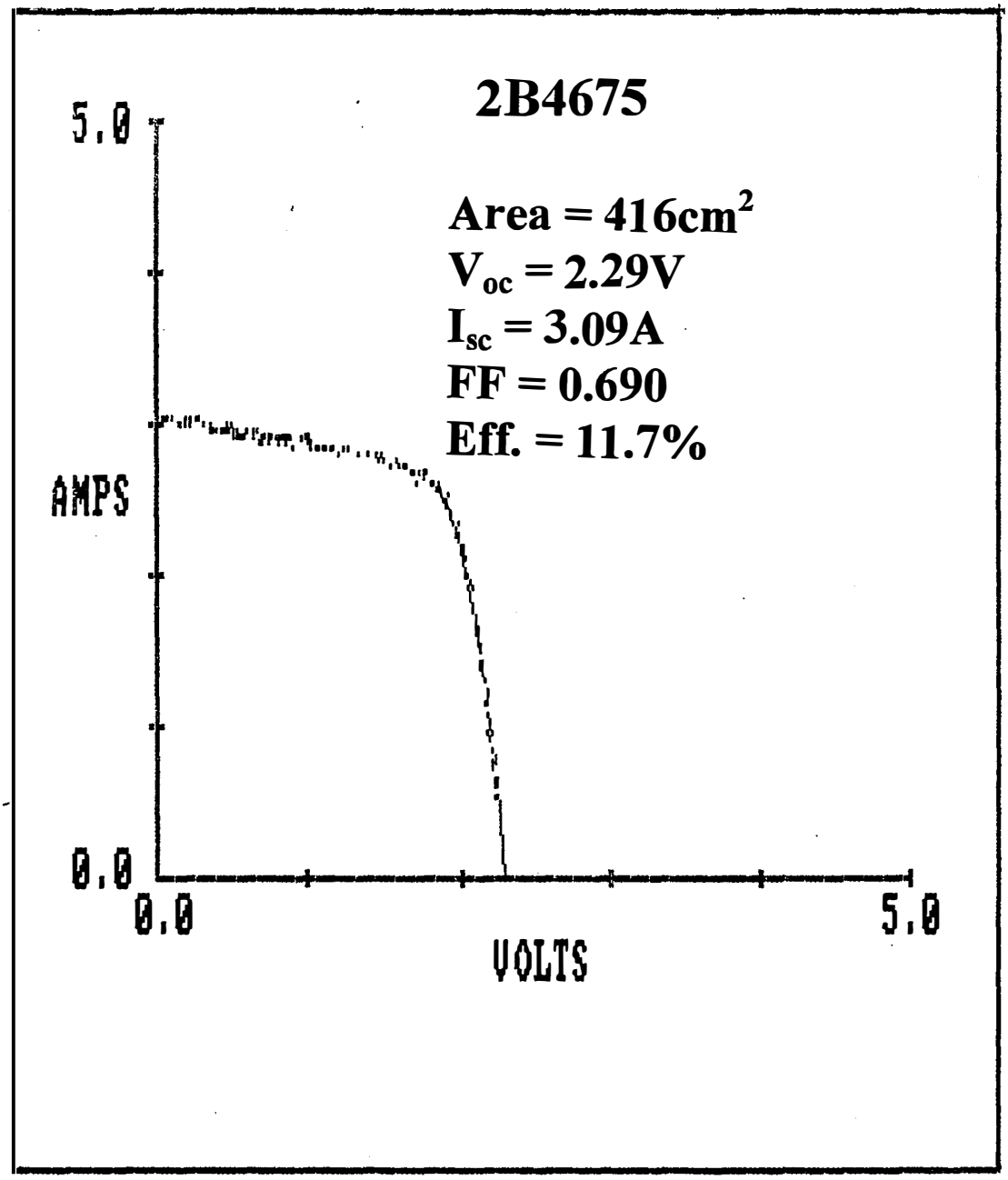


**Figure 17.** I-V characteristics of 11.7% initial efficiency module.

**Table 9. Initial Results of High Efficiency Modules.**

| Module # | Aperture area ($cm^2$) | Encapsulated Results | | | | Unencapsulated Efficiency (%) |
|---|---|---|---|---|---|---|
| | | $V_{oc}$ (V) | $I_{sc}$ (A) | FF | Eff. (%) | |
| 4661 | 415 | 2.27 | 3.08 | 0.678 | 11.4 | 11.8 |
| 4674 | 416 | 2.30 | 3.07 | 0.684 | 11.6 | 12.1 |
| 4675 | 416 | 2.29 | 3.09 | 0.690 | 11.7 | 12.0 |
| 472013 | 921 | 4.49 | 3.48 | 0.674 | 11.4 | 11.4 |
| 473219 | 922 | 4.51 | 3.44 | 0.684 | 11.5 | 11.7 |
| 476239 | 920 | 4.49 | 3.42 | 0.670 | 11.2 | 11.8 |

**Table 10. Stabilized Results of High Efficiency Modules.**

| Module # | Efficiency (%) |
|---|---|
| 4661 | 10.10 |
| 4675 | 10.24 |
| Phase III Milestone | 11.5 |

## Module Analysis

Over the course of this project, several modules of different aperture areas have been fabricated. The efficiency of the modules is usually lower than the corresponding efficiency of the small-area 0.25 $cm^2$ cells. We have carried out some studies on module-related losses and have identified some problem areas. Examples of module losses include lack of uniformity and parasitic resistance at the grid lines/ITO and grid lines/bus bar contacts. So far, we have not been able to determine the exact cause of the problems. The complexity of the module design and the many variables associated with the module fabrication make this study difficult.

In order to obtain statistical trends, we have collected data from all the modules of different areas fabricated and plotted the results graphically. The plots of series resistance, $R_s$, fill factor, FF, short-circuit current density, $J_{sc}$, and efficiency as a function of module area are shown in Fig. 18. All the modules have the triple-junction triple-bandgap configuration. The range of module areas investigated is approximately 40 $cm^2$ to 1000 $cm^2$. The values of $R_s$ and $J_{sc}$ have been calculated by normalizing the actual values of series resistance and short-circuit current of the modules with respect to module area. The figure shows that there is a spread in the values of the cell parameters for all the different module areas. The spread in FF, $J_{sc}$, and efficiency is the least for the 40-45 $cm^2$ area and highest for the 900-970 $cm^2$ area indicating that the smaller area results are more reproducible. The large spread in the value of $J_{sc}$ for the small areas is attributed to intentional changes in the top cell thickness. Also, the efficiency is the highest for small-area modules, which suggests that there is a loss due to uniformity problems.

The data in Fig. 18 have been replotted in Fig. 19 which shows graphs of efficiency versus $J_{sc}$, efficiency versus $R_s$, efficiency versus FF, and FF versus $R_s$. In each case, a second order polynomial fit trend line has been superimposed as a solid curve. It is clear from Fig. 19 that the module efficiency increases with increasing $J_{sc}$ and FF and decreasing $R_s$. The values of FF and $R_s$ also show a correlation: lower $R_s$ leads to higher FF, which is expected anyway. Based on Fig. 19, it may be concluded that two possible ways to increase the module efficiency are to further increase the $J_{sc}$ and reduce the series resistance component. The value of $J_{sc}$ may be increased by increasing the top cell thickness. More work is necessary to understand the series resistance component.

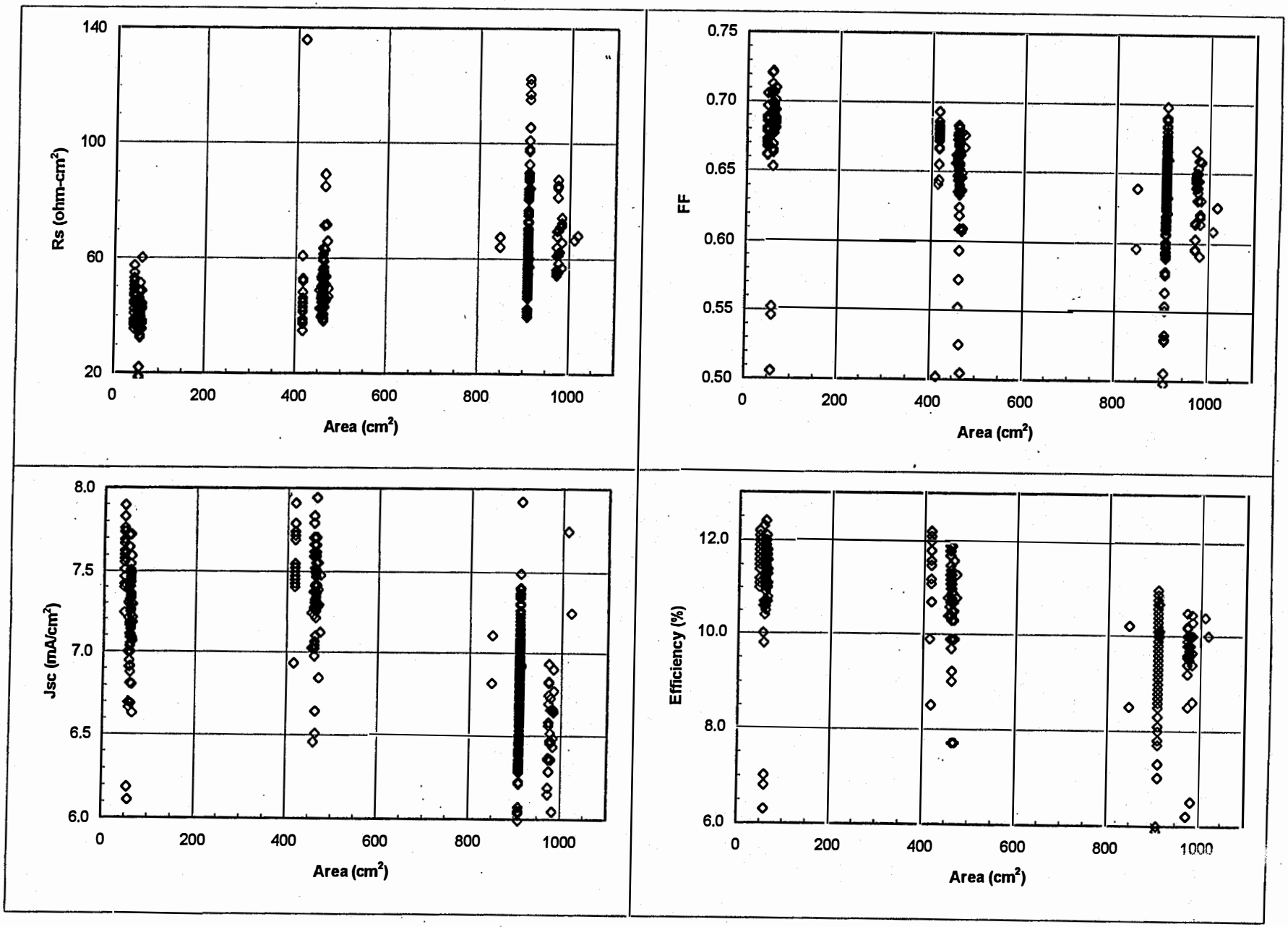


**Figure 18. Plot of series resistance Rs, fill factor FF, short-circuit current density Jsc, and efficiency as a function of module area**

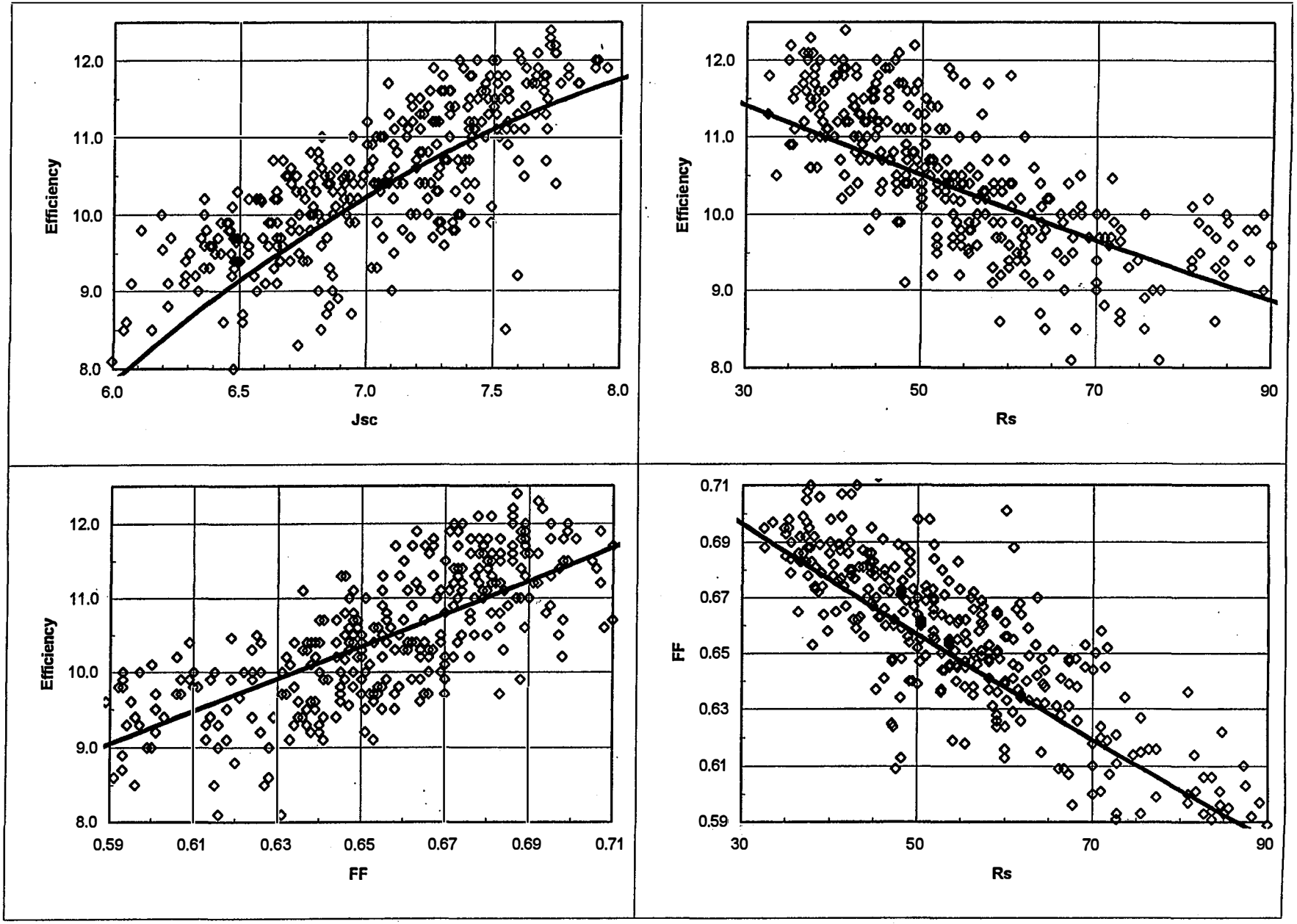


Figure 19. Plots of efficiency versus Jsc, efficiency versus Rs, efficiency versus FF, and FF versus Rs for different module areas.

# Section 5

# Laser-Processed Module Status

## Introduction

In order to reduce the cost of module manufacturing, we need to increase the degree of automation, decrease the cost of module finishing materials, and increase module efficiency. First, a cost reduction in module manufacturing may be accomplished by simply extending the roll-to-roll process as far into the module fabrication line as possible. We may also reduce the cost of module manufacturing by using less expensive materials or reducing the amount of materials utilized. Finally, an increase in efficiency, achieved by a reduction in module parasitic losses, will serve as a cost reducer.

To accomplish these goals, we are developing a laser-interconnected monolithic module process. This laser process has advantages over present fabrication designs in terms of both cost and efficiency. The cost of modules using this laser process will be dramatically reduced because of the high degree of automation obtainable because of the extension of the roll-to-roll process further into the manufacturing line. Also, because of the very small feature heights for this type of module, it will be possible to consider less expensive, more reliable alternative encapsulations that are not possible in the present module designs. The modules produced by this laser process have considerably less module losses (shadow, electrical resistance) than present modules, thus making them more efficient. The total module losses can be reduced to near 1% using this approach.

## Laser-processed Module

### *Module Design*

In Fig. 20 we show the laser device fabrication process. This module is a parallel laser-interconnected device, unlike other laser-interconnected modules that facilitate series cell interconnections. We begin the process by depositing an insulating layer onto the stainless steel substrate. This layer could be made of many materials, but we have chosen a silicon oxide alloy deposited at high rates in a CVD process. We next deposit the back reflector onto the insulator. We now have a back reflector that is electrically isolated from the stainless steel substrate forming a metal-insulator-metal (MIM) structure. We next drill a matrix of holes, arranged across the surface, through the back reflector and insulator. The back reflector must be cut back further than the insulator such that the diameter of the back reflector hole is larger and approximately concentric with the smaller insulator hole. Therefore, we still have an electrically isolated MIM structure. This is achieved with a single laser pulse. We next deposit the a-Si alloy triple-junction device. This is followed by drilling a second concentric hole through the a-Si alloy device, thereby exposing the stainless steel substrate. The diameter of this hole will be less than the diameter of the back reflector hole to maintain electrical isolation. The next step is to deposit a transparent conducting oxide over the entire surface. The TCO then makes electrical contact to the stainless steel substrate. Finally, we are then able to encapsulate the surface with a thin-film clear coat, again a CVD deposited silicon oxide alloy or a thin layer of EVA and Tefzel.

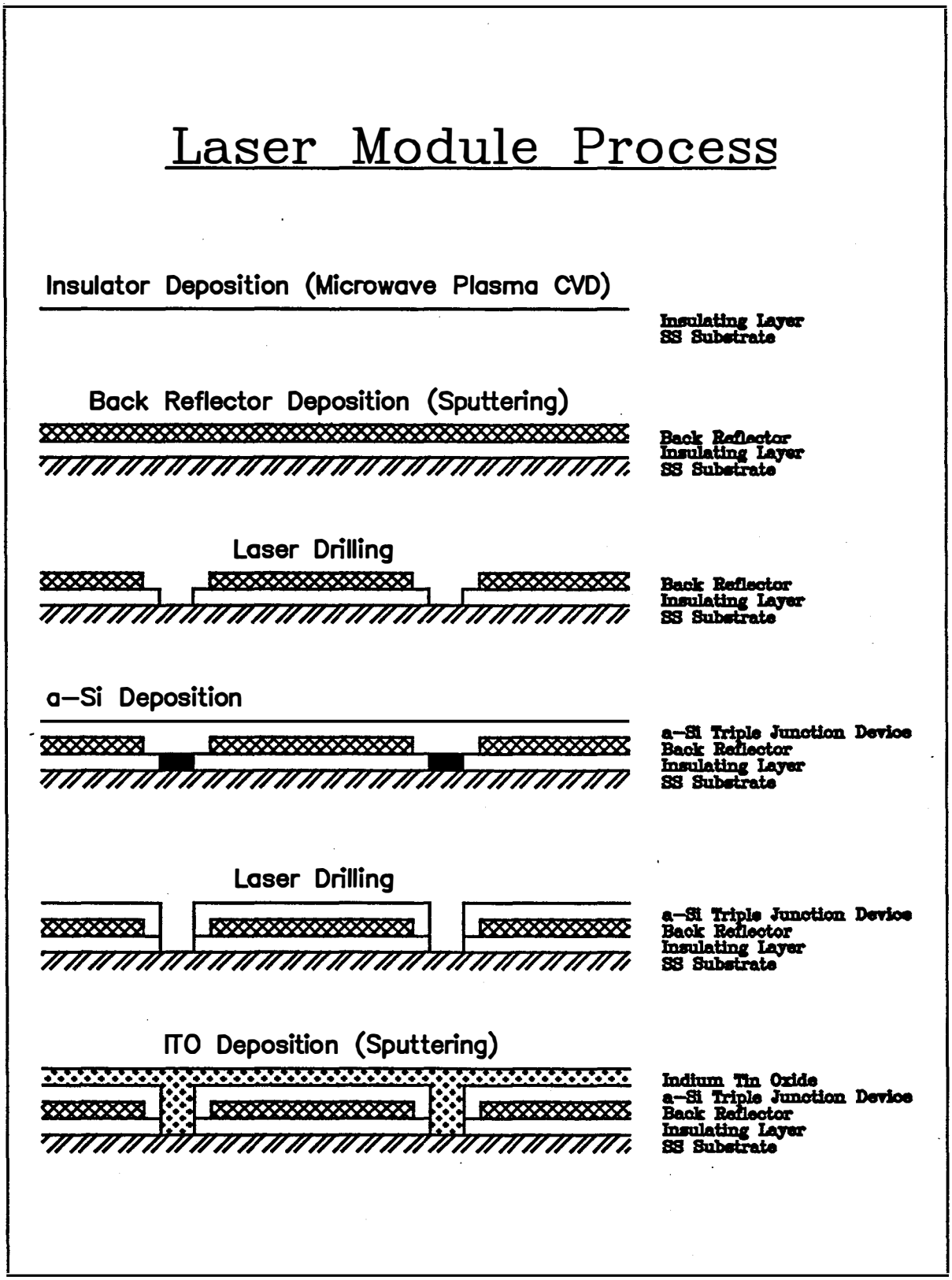


**Figure 20. Fabrication process for the laser-interconnected module.**

The electrical conduction paths are provided by the TCO and back reflector. The current is collected from the device along the surface by the TCO to the hole and down to the stainless steel now acting as the positive electrode. At the bottom of the device, current is collected from the device and traverses along the back reflector to either edge of the module to the negative electrode. In Fig. 21 we show a multi-plan view of the finished device. It can be seen from the figure that the negative electrode connection takes place on the edge of the module where the back reflector is exposed, either by masking or etching of subsequent depositions.

Given the diameter of the holes at less than 100 μm and hole spacing of 2 mm, we have achieved a shadowing loss of approximately 0.2%. These values, combined with the electrical losses due to transport of current across the TCO and back reflector sheets, give us a total electrical and shadow loss of approximately 1%.

The layout design of the one-square-foot laser-interconnected module is shown in Fig. 22. This drawing shows the laser patterning and thin-film deposition borders as well as contacts. We have fabricated shadow masks for the BR, a-Si, ITO and contact layer depositions to provide access to the BR contacts as well as isolation of the top contact from the BR.

For our prototype module, we start with a piece of .005" thick stainless steel cut to 14" wide by 15.25". We will next punch ¼" registration holes to align the shadow masks in the thin-film deposition processes. The insulator/BR films are then deposited. These films extend out beyond the a-Si alloy device by about 5/8" on two opposite sides in order to trim the tapered edges of the insulator/BR and establish the negative contact to the BR. Contact pads are then deposited on these exposed edges. The pads are segmented to allow for electrical isolation of the back reflector into strips if desired.

The first laser processing occurs after completion of the ss/insulator/BR and contact pads. This involves cutting continuous lines to segment the BR into sections, if necessary, and drilling through holes into the BR at an appropriate spacing using the laser processor described above. The a-Si alloy device is deposited in-board the BR on the two edges with contacts and flush to the BR on the other two sides. The device is then laser processed by drilling a second set of holes concentric with the BR holes over the entire square foot. The last process is that of depositing the ITO top contact. This layer is deposited completely inside the perimeter of the a-Si alloy device deposition as shown in Fig. 22, completing the thin-film depositions.

The module is then finished by etching a boarder in the ITO layer, if necessary, and passivation of the device. The output interconnects are made on the contact pads on the two sides of the module. These contacts will be tied together and brought out as output leads. Finally, the module is encapsulated in an EVA/Tefzel lamination.

## *Laser Processing*

After the MIM is deposited, we drill holes through the back reflector and insulating layers. This is done with a Nd:YAG laser operating in the Q-switched single shot mode. We are utilizing the laser at its fundamental wavelength at 1.064 μm. The Ag/ZnO layers are vaporized by the laser in the initial part of the pulse. The fact that the silver is textured and has ZnO on the top allows it to absorb the laser radiation at the laser wavelength. The insulating layer does not readily absorb the radiation but primarily transmits it to the stainless steel substrate. The surface of the substrate material is vaporized, thereby ablating the insulating layer above it. This process occurs later in the same laser pulse. As a result of the Ag/ZnO layer being vaporized first, it is vaporized to a larger diameter (where the energy from the beam is less intense) than the insulator ablated diameter.

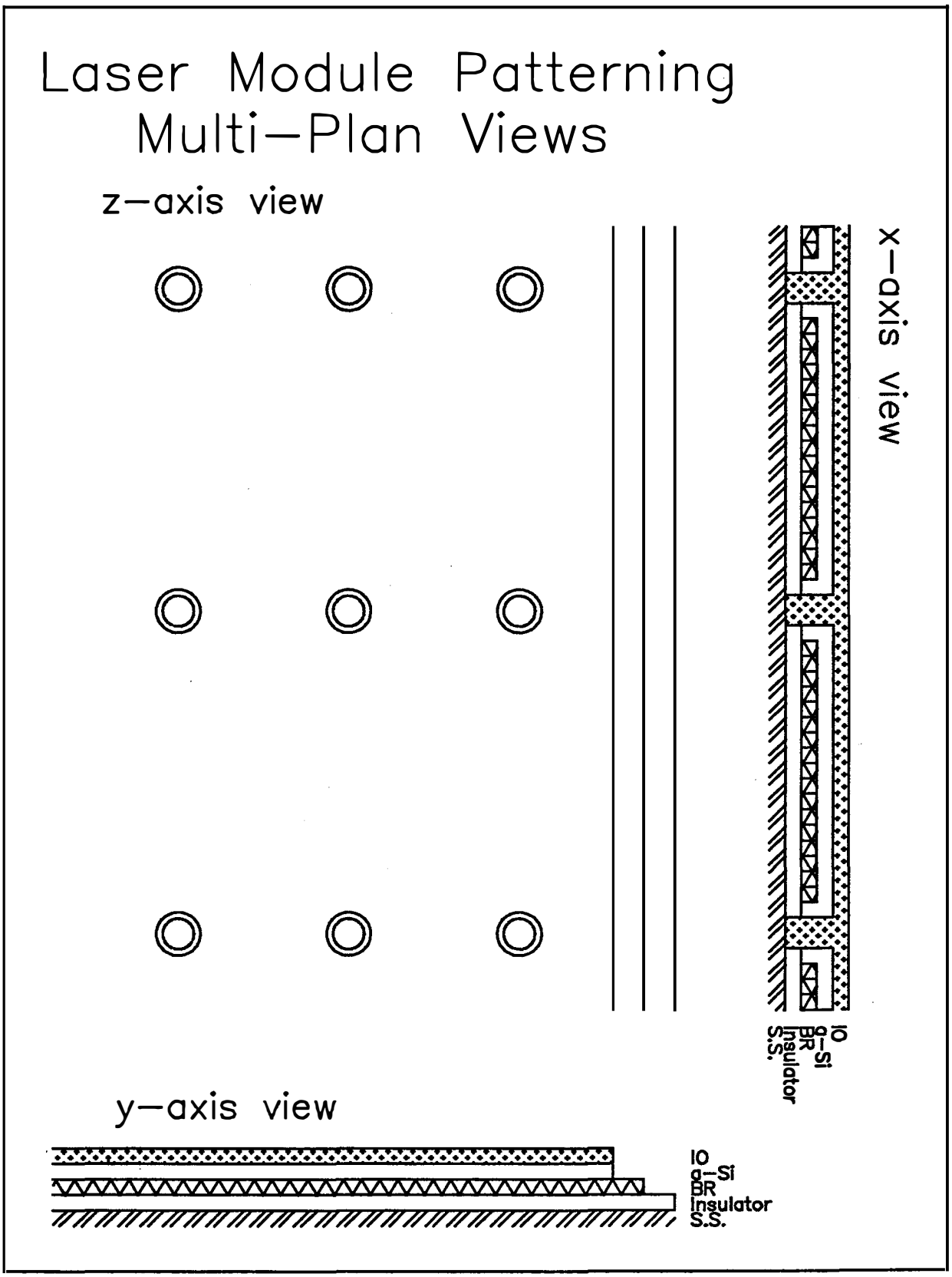


**Figure 21. Multi-plan view for the laser-interconnected module.**

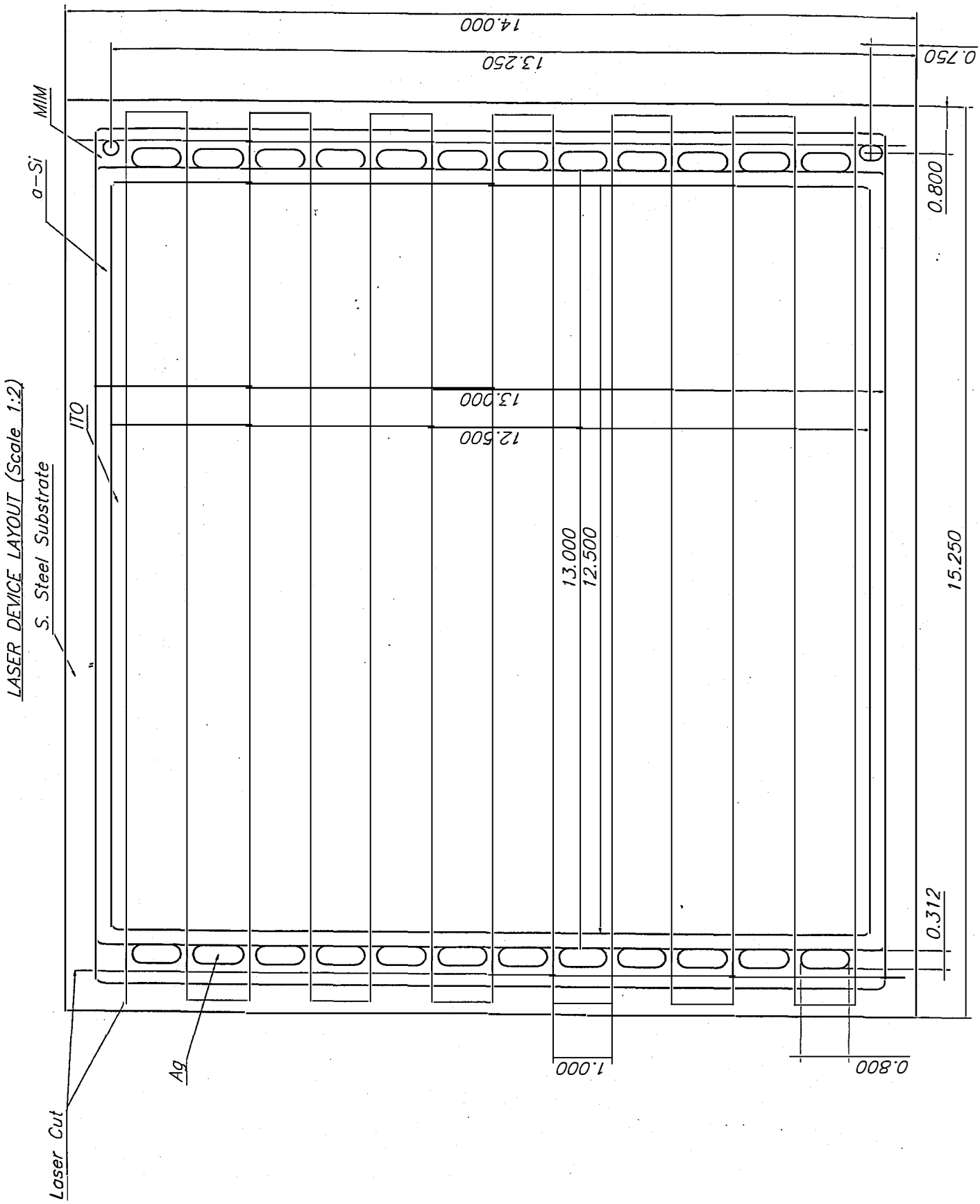


**Figure 22. Layout diagram for laser-Interconnectaed module.**

In Figs. 23a and 23b we show SEM photographs of a laser-drilled hole in the MIM structure. In Fig. 23a the outermost diameter hole is where the back reflector has been cut back. The diameter of this hole is approximately 100 μm. Inside of this diameter there is a crater-like hole with a rim. This is the exposed stainless steel with the rim being molten material pushed out from the center of the hole. The relatively smooth region between the remaining back reflector and the center hole is the insulating layer being exposed. Figure 23b shows the same hole at a large oblique angle to demonstrate the absence of large thrown debris on the surface. The largest feature heights on this surface are about 1 μm or less.

After we have laser etched holes in the MIM film structure, we deposit the a-Si alloy device. Once the device has been deposited, we drill a second hole that is concentric within the first hole. The diameter of this hole is typically 30-40 μm in diameter. Again, this is an ablation process since the a-Si alloy does not absorb the laser radiation readily. Here the stainless steel is vaporized, removing the a-Si alloy layer above it. Finally, the TCO layer is deposited completing the device by making contact through to the stainless steel for the positive electrode. The negative electrode is the back reflector and is contacted near the edge of the device.

Fig. 24 shows a SEM photograph of a device after it is completed (after TCO deposition). Again, the outermost diameter is the back reflector, as it is apparent through the a-Si alloy device and TCO because of the conformity of both layers. The next diameter, with the rim, is the first exposure of the stainless steel substrate. The innermost diameter, with rim, is the second exposure of the stainless steel (as seen through the TCO) from the a-Si alloy cut. In this hole there is TCO on top of the exposed stainless steel.

The accuracy of the second cut is paramount to the finished device. The acceptable position is such that the second hole lies completely inside the outermost diameter, i.e., the back reflector cut. The result of any part of the hole cut over the back reflector area might result in a shunt path from the TCO to the back reflector. We presently use a precision x-y motion table with sufficient accuracy to reproduce the second cut. We believe this type of accuracy is readily obtainable over large areas with present positioning technology.

### *Insulator*

The success of the laser-interconnected module is dependent on the development of thin transparent insulating films. We have chosen a clear-coat material composed of a silicon oxide alloy possessing high optical transparency, high electrical resistivity, and low water permeation. This layer will be used, as described above, as the insulator between the ss substrate and the BR films. To achieve this, we have designed and built a large-area microwave frequency energized plasma CVD system which is capable of depositing the clear-coat film at rates in excess of 100 Å/s. The schematic diagram of the machine is shown in Fig. 25.

The microwave energy is fed into the deposition chamber using a linear applicator. The deposition frequency is 2.45 GHz and the power is variable up to 7 kW. The deposition gasses include $SiH_4$, Ar, $CH_4$, $N_2$, and $O_2$. The vacuum system can handle a total gas flow of up to 2000 sccm while maintaining a pressure to a few microns in the chamber. The chamber is pumped by two 20" diffusion pumps backed by a mechanical pump. The machine design provides uniform deposition over an area of approximately 1 square foot. Thus far, we have achieved a thickness uniformity of 5% over this area.

We have fabricated metal-insulator-metal structures utilizing the μ-wave CVD silicon oxide films to test the isolation of the two metal contacts (s.s and BR). We have been consistently able to achieve resistances of greater than 1 MΩ-cm$^2$ over an area of 1000 cm$^2$. This resistance exceeds the load line of a triple cell by about a factor 3000, resulting in shunt loses of less than 0.1%.

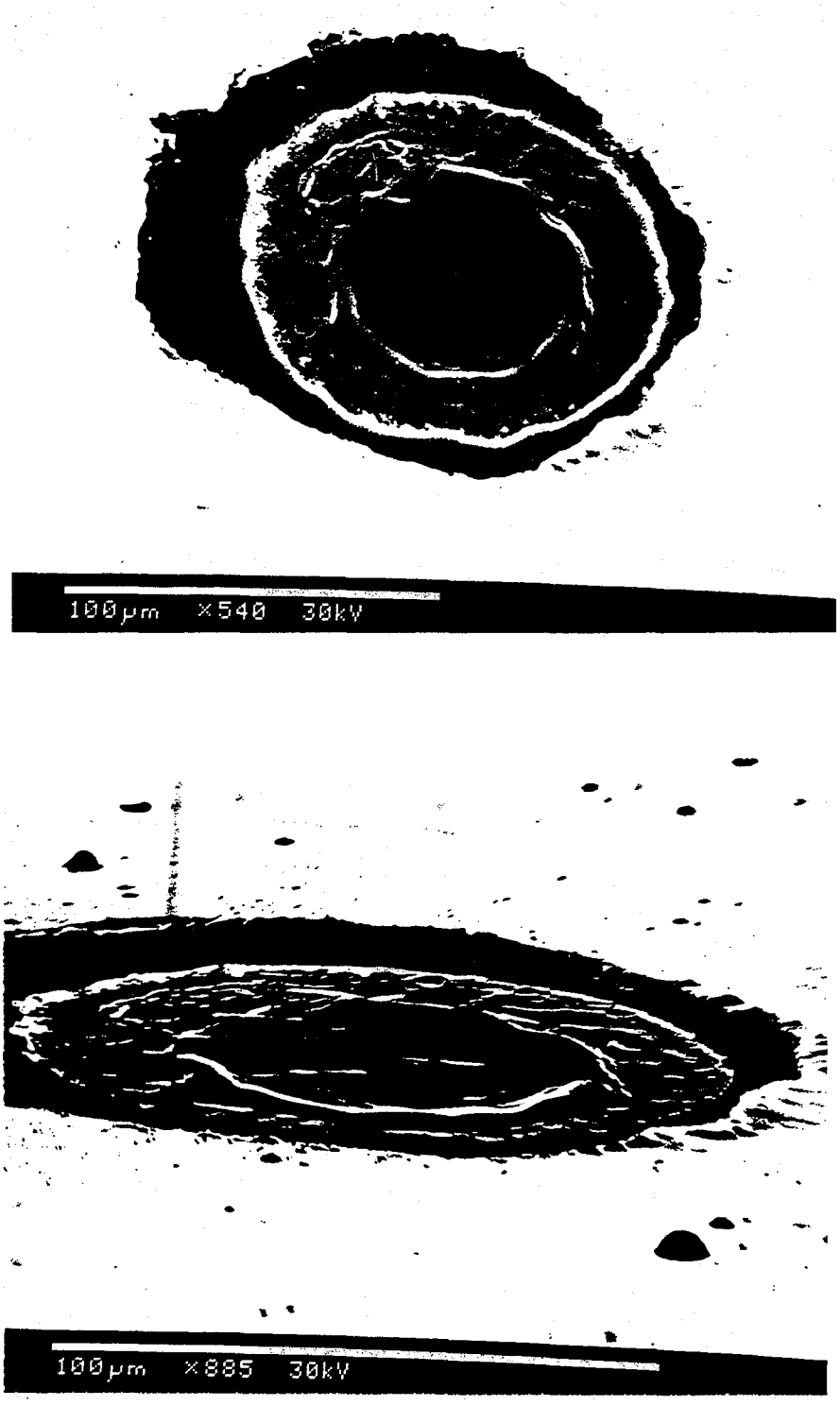


**Figure 23.** **SEM photographs of a) a laser ablated hole in a MIM structure and b) the same hole at a large oblique angle.**

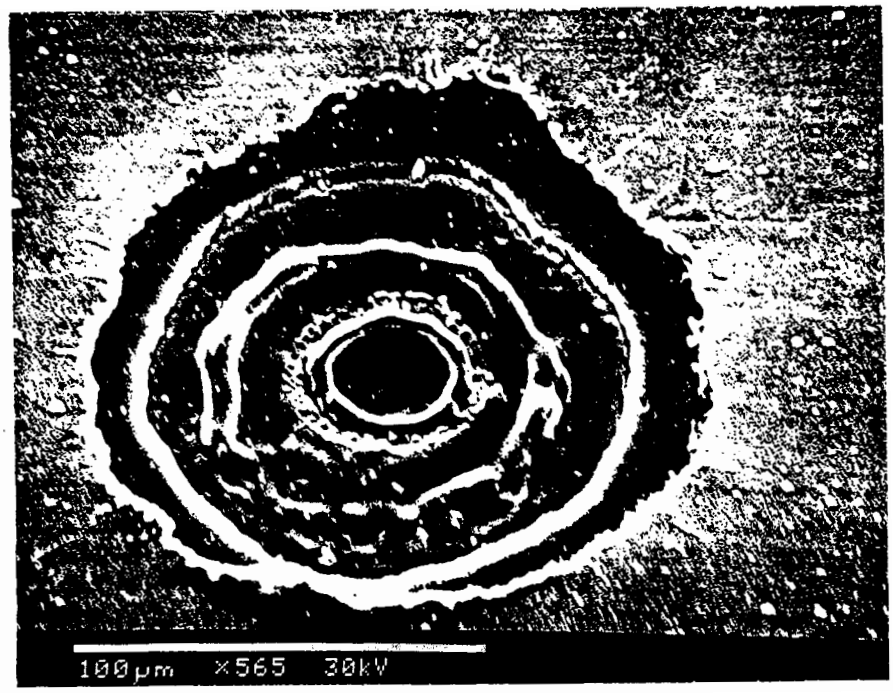


**Figure 24. A laser hole in a finished device.**

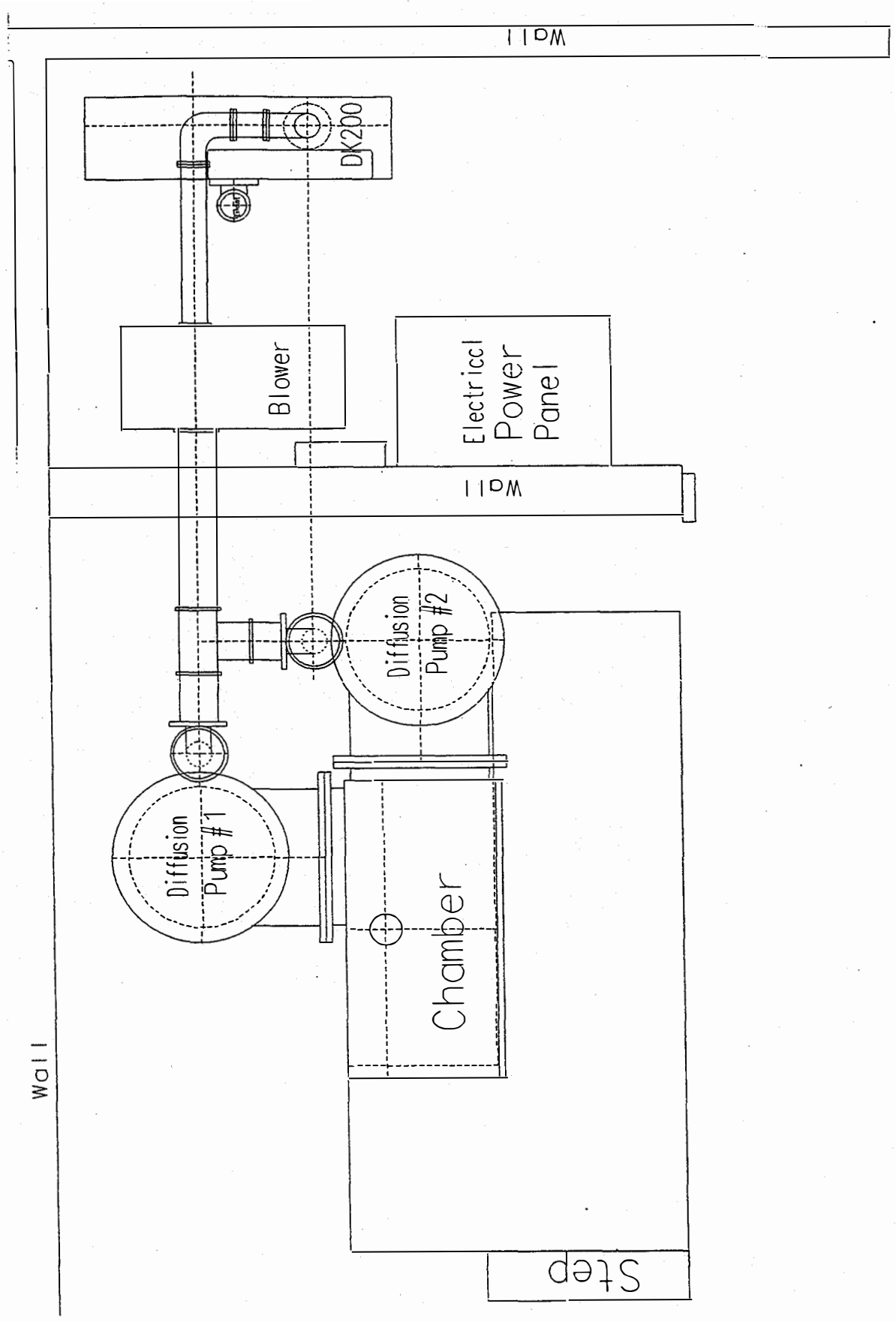


**Figure 25. Schematic diagram of the insulator/clear-coat machine.**

### *Effect of Thrown Material on Device Performance*

Much work has been done on optimizing the laser power, laser beam size and focus diameter as well as individual film thicknesses to optimize the drilling of the laser hole. This hole must be cut with a minimum of material thrown onto the back reflector surface. This thrown material can take two basic forms. The first is in the form of resolidified globules or debris. These can be quite large and may later contribute to shunt paths through the device from the back reflector to the top TCO contact and therefore must be minimized. The second problem caused by thrown material is on the molecular or atomic level where a film is deposited or recast onto the back reflector surface near the hole. This may cause additional device series resistance since this film may not be conducting. This thin film of recast material may manifest itself in a reduction of the device fill factor as a result of the increased series resistance. This film may also be a source of parasitic optical absorption, reducing the effect of the back reflector to optically enhance the device current.

To study this effect, we prepared several devices on (MIM) structures with various thicknesses of insulator. For each sample we cut laser holes on half the substrate while the other half was left with no laser processing. We then deposited an a-Si alloy single cell over the entire area. This was followed by the deposition of 0.25 $cm^2$ ITO dots to define discrete devices to be tested on both areas with and without laser processing. (In this structure we did not cut holes through the a-Si alloy device before depositing ITO as we do in the complete laser-connected devices.) Any film deposited by thrown material during the laser process that adhere to the back reflector (BR) would produce a barrier layer between the BR and the $n^+$ layer of the device. This test structure allows us to look at the effect of the laser cut and material recast layers on device performance. This is done by measuring the I-V characteristics and comparing the results of devices built on the laser-processed half of the sample with those on the unprocessed half.

To help minimize recast onto the surface of the sample in our laser processing system, we utilize inert gas jets focused on the point of the laser strike. This technique is very effective in removing recast without causing other unwanted effects. We have found, however, that this is still not sufficient to completely prevent the recast from forming on the surface.

In Fig. 26 we show a plot of the device parameters versus insulator thickness. From the figure it is apparent that for thin insulator (5000 Å), we see almost no effect of the recast layer on device performance. This is a result of less laser power being required to completely break through the BR and insulating layers, causing less material to be thrown. With a thicker film we need higher power, throwing more material, and we see significant degradation due to this recast film. This layer degrades the fill factor through an increase in the series resistance of the device. The current is also affected, presumably due to a decrease in back reflection. The magnitude of these two effects on the device are similar.

Unfortunately, the thinner insulating layers may not be sufficient to provide consistently good device shunt resistance across the insulator. Only at insulator thicknesses of 1.5 μm do we have consistently acceptable resistance. We have been able to develop successfully a proprietary technique to completely eliminate the recast caused by laser drilling the first back reflector holes even with thicker insulator layer. Again, we built test cells consisting of a Ag/ZnO back reflector on insulator/ss. The insulator thickness on these samples was about 2.5 μm. The back reflector/insulator was then laser drilled on one half of the sample, and an a-Si alloy single cell and ITO was then deposited without a second hole drilling. This structure has allowed us to examine the effect of recast produced by the first cut. Table 1 shows the percentage difference in the I-V characteristics between the devices on the laser-processed half of the sample to devices on the unprocessed half. From the table it can be seen that the new technique had a significant effect on the I-V characteristics. There was an improvement in the series resistance and the current of the samples.

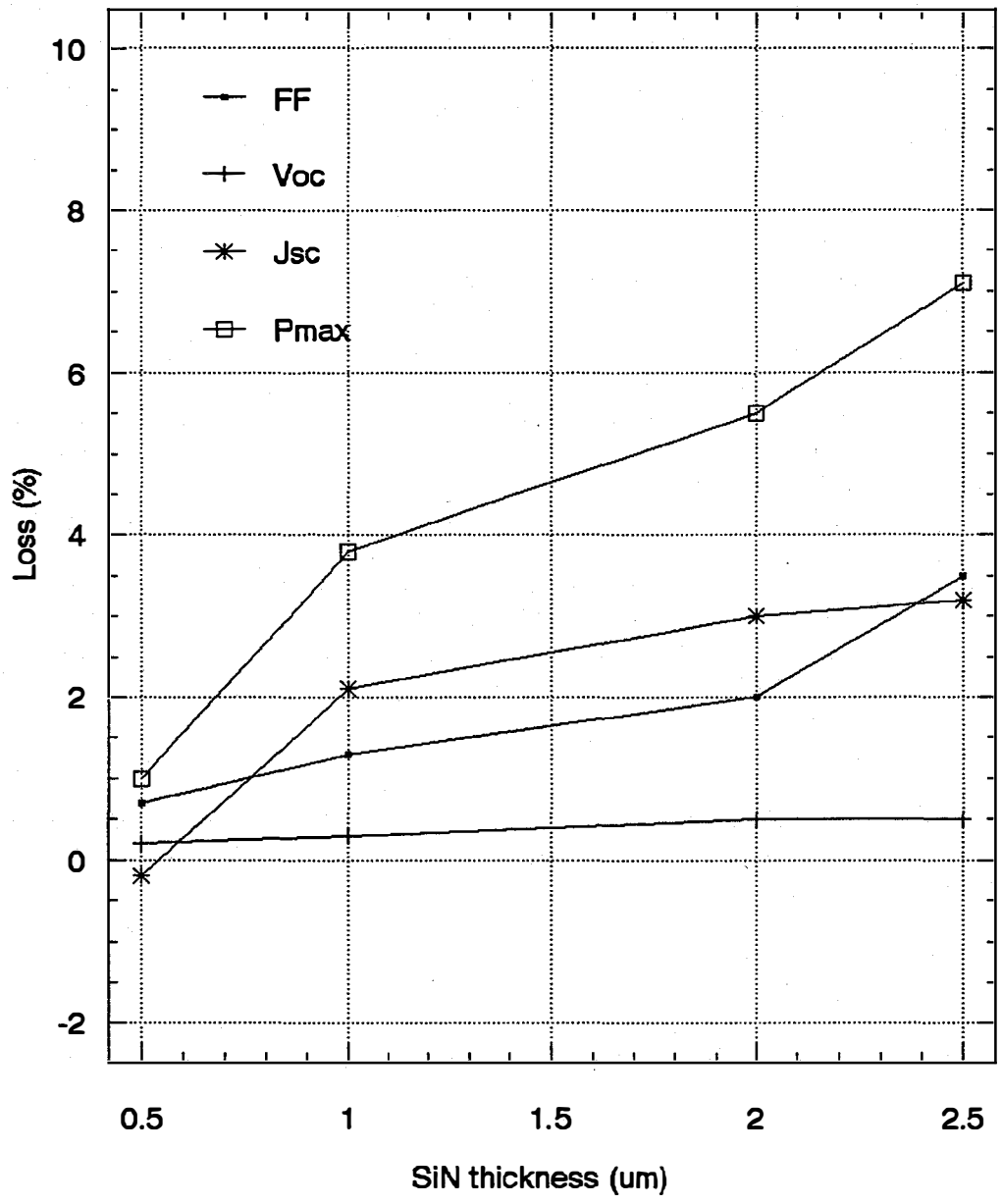


**Figure 26.** **A plot of the laser device I-V parameters versus thickness of insulator.**

### *Other Parasitic Resistances*

Even though the recast removal has been very effective in the reduction of the device series resistance, there still exists significant excess series resistance. This was determined by comparing the series resistance of the laser processed devices with the series resistance of small area devices fabricated with standard grid fingers. The series resistance of the improved device listed in Table 11 is still about 14 Ω-cm² compared to about 21 Ω-cm² before recast removal, while the small area gridded cell typically gives 6 Ω-cm².

**Table 11. Losses Due to Parasitic Recast Layer with and without New Removal Technique.**

| | Conventional | New |
|---|---|---|
| Pmax | -7.1% | -0.7% |
| ff | -3.5% | -0.1% |
| Voc | -0.5% | -0.3% |
| Jsc | -3.2% | -0.4% |

We believe there are three possible sources of extra series resistance in these laser-connected devices. These are ITO sheet resistance, recast after the second laser cut and hole contact resistance (ITO to stainless steel contact). We have repeatedly tested the effect of recast resistance due to the first laser cut and have found no contribution to the device series resistance since we have adopted the procedure to remove this material. We have modeled each of the three possible sources of resistance as a function of hole spacing and each effect has a different dependency. The total effect on series resistance can be estimated by

$$R_{excess} = \frac{R_r R_d}{R_r + R_d} s^2 + R_c s^2 + \frac{s^2 \rho_\square}{2\pi} \ln\left(\frac{s}{h}\right)$$

where $R_r$, $R_c$, $R_d$, and $\rho_\square$ are the recast, contact, device and sheet resistances respectively and s and h are the hole spacing and hole diameter. The first term is the recast resistance term, the second is contact resistance and last is sheet resistance. The final term is only dependent on ITO sheet resistance, hole spacing and hole diameter, all of which are independently measurable quantities. In the first term the device series resistance was determined independently by assuming it to be the same as in the small-area gridded sample. This leaves us with only two unknown parameters, the contact resistance, $R_c$, and the recast resistance, $R_r$ due to the second (a-Si alloy) cut.

Figure 27 shows the effect of hole spacing on the sheet, contact and recast resistance as well as on actual devices. We have measured $\rho_\square$ to be 125 Ω/□, h is about 40 μm and $R_d$ is 6 Ω-cm². In this figure we have split up the components of resistance into the three terms in the excess resistance equation. The curve labeled *Total* would then be the sum of the component resistances, namely, $R_{excess}$. We varied $R_r$ and $R_c$ to obtain a best fit (labeled *Total*) to the measured data. The curves labeled *Contact*, *ITO* and *Recast* are the component resistances obtained from a best fit to the data. It appears that the contact resistance dominates over the recast resistance. This is an important result; since the first cut causes no excess series resistance and the recast resistance of the second cut is small, we have eliminated all series resistance due to thrown material.

It is also important to note that the excess resistance expected from the laser device structure, even if the contact and recast resistance were to be eliminated completely, is several ohm-cm² even for relatively close hole spacing. This extra resistance is only significant for a single-junction device. For a triple-junction device this excess series resistance would have almost no effect on the fill factor of the device.

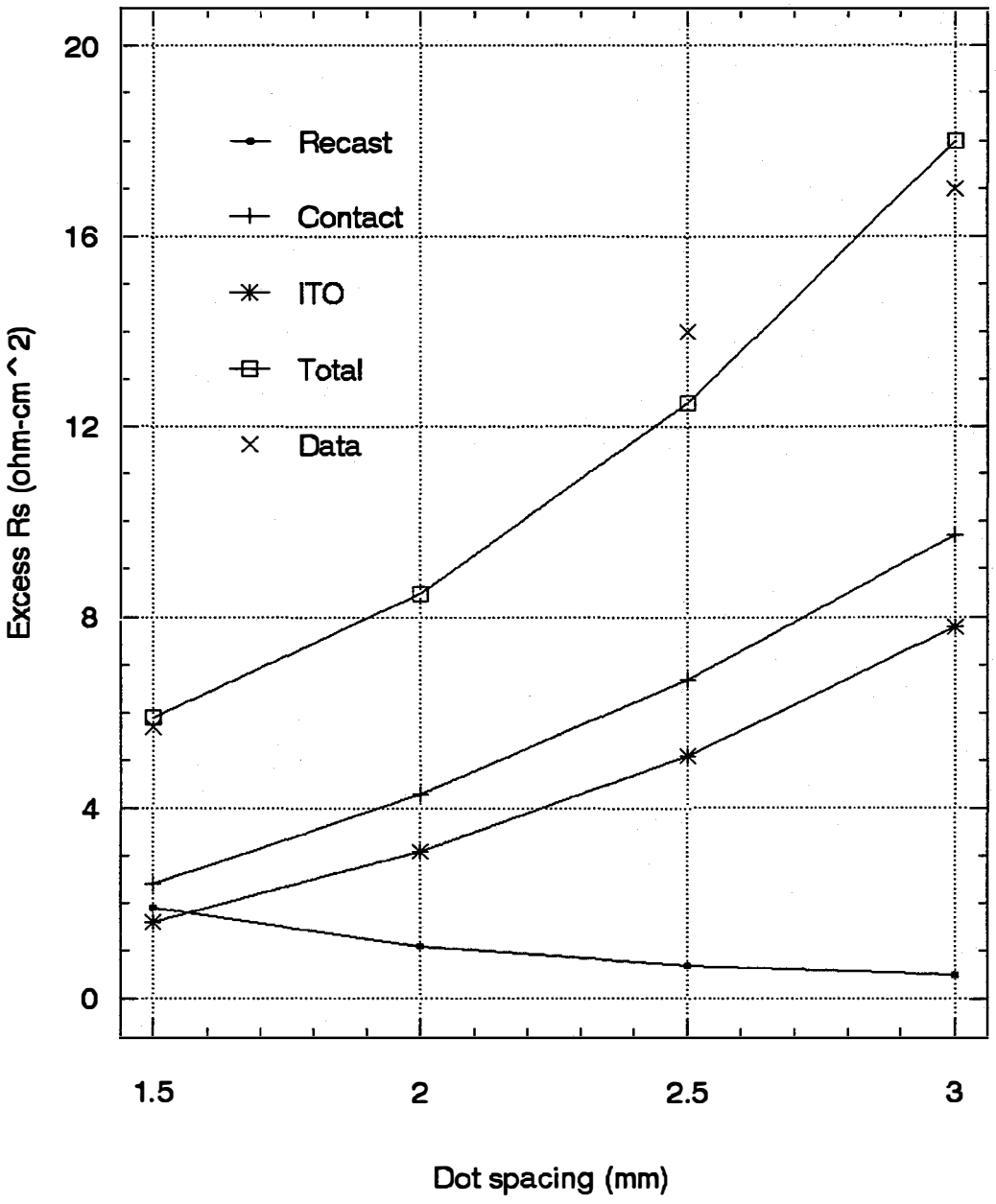


**Figure 27.** **Excess device series resistance and its component resistances as a function of laser hole spacing.**

## Results

We have fabricated a laser-processed module with an efficiency of 10.6%, shown in Fig. 28. This module had a series resistance of 59 $\Omega$-cm$^2$ compared to approximately 45 $\Omega$-cm$^2$ for a conventional gridded module of similar area. This has resulted in a fill factor that is about 10-15% lower for the laser-processed module. The current density is approximately 7% higher than the convention module as a result of the lower shadowing loss. The shadowing loss for the laser module (area of point contacts) is only 0.5%. On a small area device, 12.6 cm$^2$ we have achieved an efficiency of 11.5%, shown in Fig. 29.

Although we still have room for improvement with this module design we have made significant progress in many areas. We have produced a pin-hole free insulating layers that are capable of isolating the back reflector from the stainless steel substrate with resistances of greater than 1 M$\Omega$-cm$^2$. We have consistently been able to produce these high quality insulating layers run after run. We have developed a high speed laser scanning system that is capable of drilling hundreds of holes per second through the various thin-films with micron accuracy. We have identified and minimized the effect of parasitic losses in the module, such as elimination of recast and debris formation and their effect on device performance. We have dramatically increased the yield of these modules by the reduction of shunting effects. We have also greatly decreased the resistance of the point contact (ITO/s.s interface) to a level that we are approaching the module sheet resistance of the conventional gridded module. This last area is the area of which future improvements can be made.

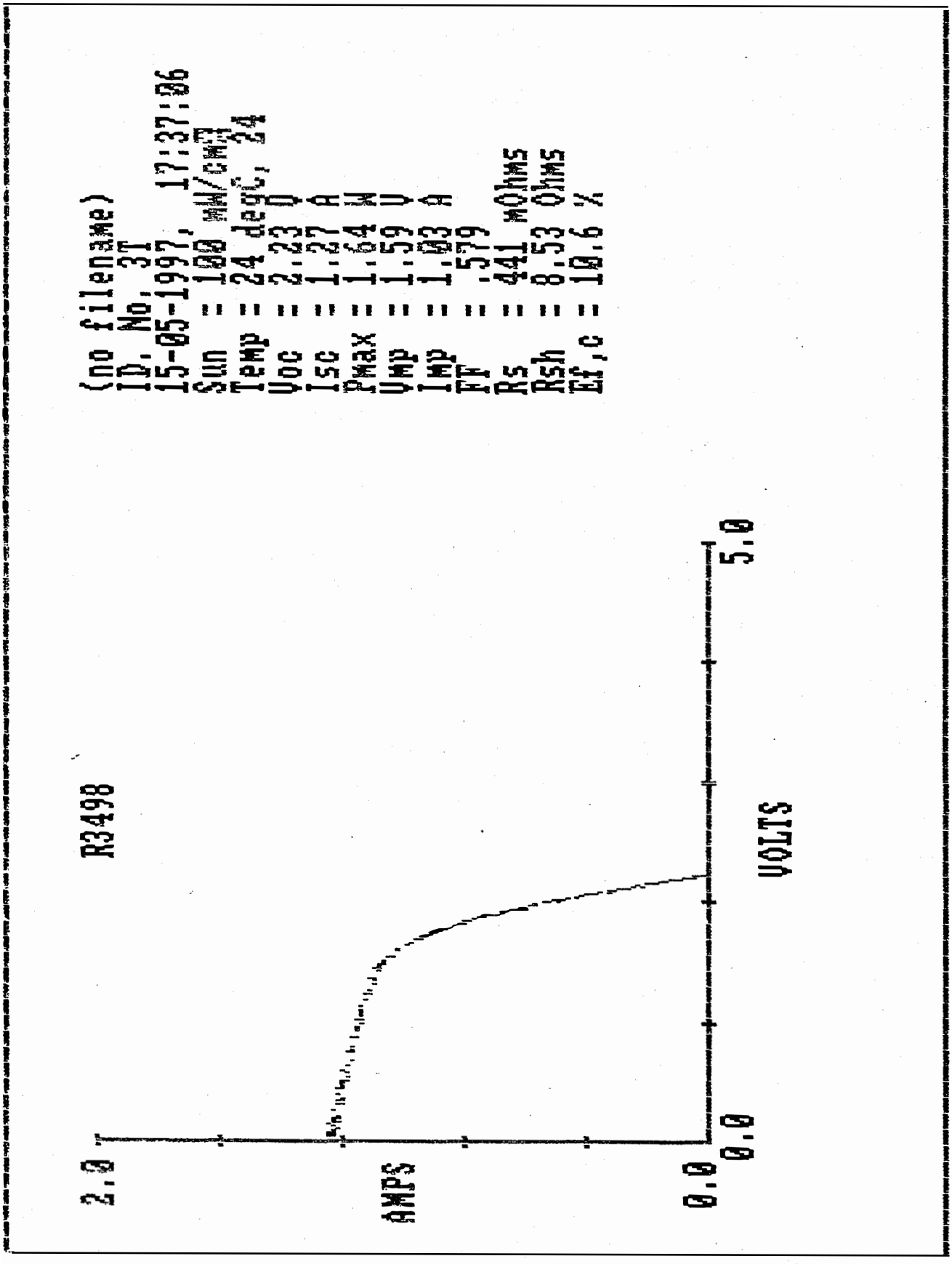


**Figure 28.** **Initial I-V characteristics of an 10.6% laser-interconnected triple-junction module.**

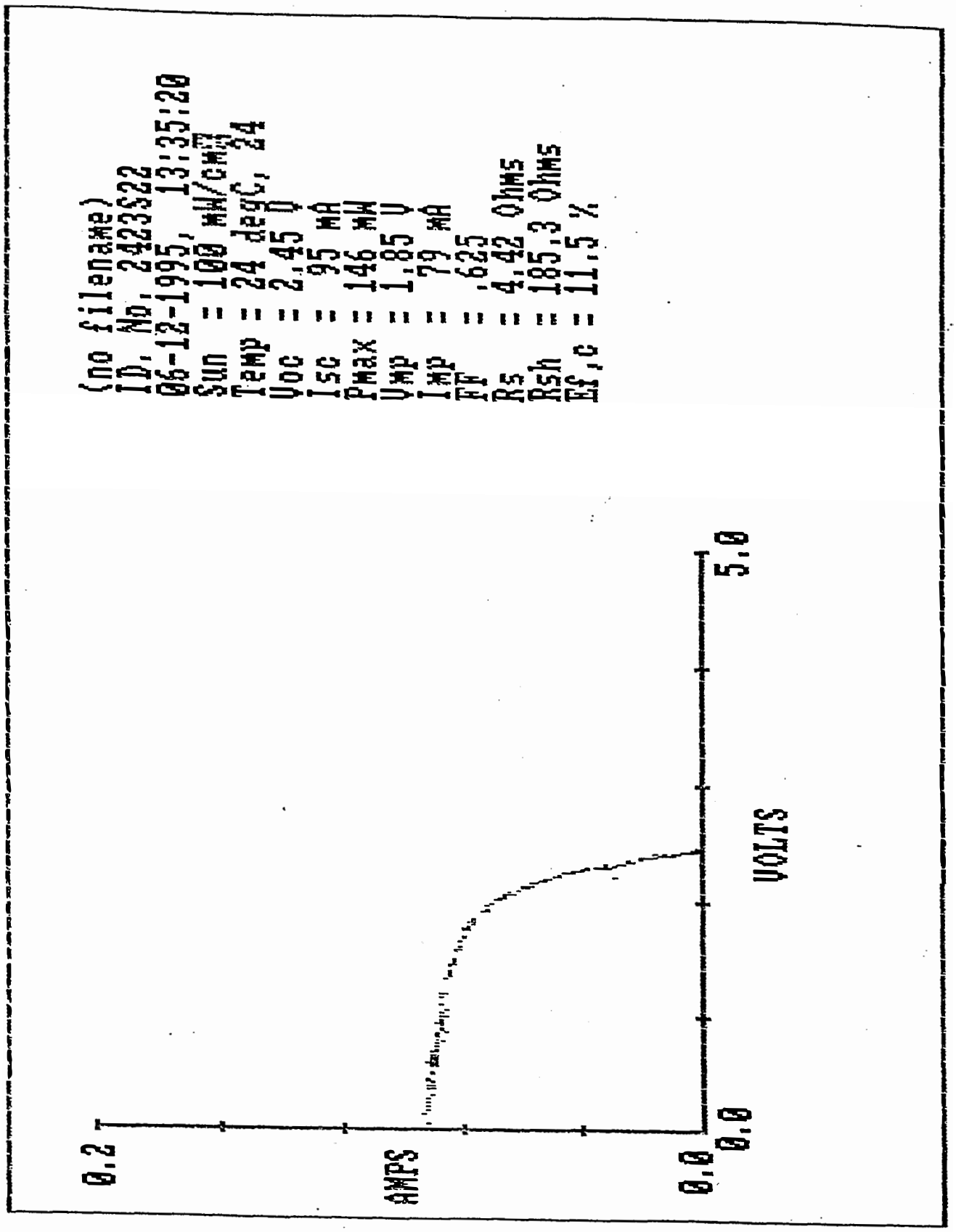


**Figure 29.** **Initial I-V characteristics of an 11.5% laser-interconnected triple-junction device.**

# Section 6

# Reliability Testing

## Introduction

We have been testing our modules following IEEE PAR 1262 (Draft 8) which is more stringent than the NREL Interim Qualification Test (NREL/TR-213-3624). The detailed test sequence is shown in Table 12. Three different configurations were used for the test: (1) L-strip laminate on Ag/ZnO back reflector which is essentially a monolithic encapsulated module of area 24 by 36 $cm^2$, (2) 1 ft. by 4 ft. 10-strip interconnected encapsulated module on Al/ZnO back reflector and (3) 1 ft. by 4 ft. 10-strip interconnected encapsulated module on Ag/ZnO back reflector. The results of the tests are shown in Tables 13-15. Some important observations are given below.

Our production modules have passed all the tests. The 2B modules, which have a similar design, are therefore expected to pass the test, too. Results of "heat cycling," "heat," and thermal cycling tests are reported.

## Initial Tests

All modules pass the initial tests specified in Table 12. Please note that the Spire simulator was recalibrated since the lamp was changed after the first measurement, and the modules were measured both before (b.1) and after. Note that the new values are about 4-5% lower (Table 13).

## Sequence B Tests

The results are shown in Table 14. Note that no UV test was done.

*Thermal Cycles*

All the modules pass the thermal cycles.

*Humidity/freeze Cycles*

The modules showed increase in the leakage current after the test. The magnitude of the leakage current and also the power output were acceptable and met the acceptance criteria.

*Surface Cut Susceptibility*

The modules passed the cut tests.

**Table 12. Summary of "Heat Cycling" of TA2 and 2B Modules after 180 Cycles.**

| Module | Status | $V_{oc}$ (V) | $I_{sc}$ (A) | FF | $P_{max}$ (W) | Efficiency (%) | Degradation in $P_{max}$ (%) |
|---|---|---|---|---|---|---|---|
| TA 172 | Initial | 1.77 | 5.67 | .652 | 6.54 | 7.2 | |
| | Final | 1.80 | 5.60 | .652 | 6.58 | 7.2 | +0.6 |
| TA 174 | Initial | 1.76 | 5.62 | .658 | 6.53 | 7.2 | |
| | Final | 1.78 | 5.56 | .654 | 6.48 | 7.1 | -0.8 |
| TA 176 | Initial | 1.77 | 6.14 | .651 | 7.07 | 7.2 | |
| | Final | 1.78 | 6.13 | .642 | 7.01 | 7.2 | -0.8 |
| 2B 3972 | Initial | 2.34 | 6.24 | .650 | 9.49 | 9.7 | |
| | Final | 2.34 | 6.18 | .641 | 9.27 | 9.5 | -2.3 |
| 2B 3987 | Initial | 2.33 | 6.46 | .657 | 9.88 | 10.1 | |
| | Final | 2.33 | 6.37 | .656 | 9.73 | 10.0 | -1.5 |
| 2B 4014 | Initial | 2.31 | 5.92 | .655 | 8.97 | 9.9 | |
| | Final | 2.34 | 5.86 | .651 | 8.91 | 9.8 | -0.7 |
| 2B 4016 | Initial | 2.32 | 5.88 | .670 | 9.15 | 10.1 | |
| | Final | 2.34 | 5.82 | .664 | 9.06 | 10.0 | -1.0 |
| 2B 4036 | Initial | 2.29 | 5.88 | .642 | 8.64 | 9.5 | |
| | Final | 2.27 | 5.76 | .608 | 7.94 | 8.7 | -8.1 |

## Table 13. Module Performance After Dry and Wet Highpot Tests.

| | | | Initial Tests: (watts) | | (micro-amps) | | (watts) | | | redo | |
|---|---|---|---|---|---|---|---|---|---|---|---|
| | Type | Ser.# | Pmax (b.l.) | Voc(1 klux) | dry Hipot | wet Hipot | Pmax (init) | P/P(b.l.) | Voc(1 klux) | Pmax (init) | P/P(b.l.) |
| L-strip | (Ag) | 212 | 7.09* | 1.47 | | 0.5 | 7.16* | 1.0099 | 1.47 | | |
| L-strip | (Ag) | 214 | 7.1* | 1.47 | | 0 | 7.11* | 1.0014 | 1.48 | | |
| L-strip | (Ag) | 217 | 7.12* | 1.47 | | 0 | 7.13* | 1.0014 | 1.45 | | |
| L-strip | (Ag) | 218 | 7.12* | 1.47 | | 0 | 7.06* | 0.9916 | 1.47 | | |
| L-strip | (Ag) | 219 | 7.06* | 1.46 | | 0.5 | 7.08* | 1.0028 | 1.47 | | |
| 1'x4' | (Al) | C1 | 35.93* | 14.1 | 0.5 | O.L. | 36.36* | 1.012 | | 34.5 | 0.9602 |
| 1'x4' | (Al) | C2 | 34.55* | 14 | 0.5 | 4 | 34.78* | 1.0067 | | | |
| 1'x4' | (Al) | C3 | 36.5* | 14.1 | 0 | 3 | 36.64* | 1.0038 | | | |
| 1'x4' | (Al) | C4 | 36.17* | 14.1 | 0.5 | 4 | 36.13* | 0.9989 | | | |
| 1'x4' | (Al) | C5 | 37.11* | 14.1 | 0.5 | 3 | 36.98* | 0.9965 | | | |
| 1'x4' | (Ag) | U1 | 32.04* | 10.4 | 0 | 3 | 32.14* | 1.0031 | | | |
| 1'x4' | (Ag) | U2 | 31.21* | 10.4 | 0 | 2 | 31.69* | 1.0154 | | | |
| 1'x4' | (Ag) | U3 | 40.87* | 13.3 | 0 | 3 | 40.94* | 1.0017 | | | |
| 1'x4' | (Ag) | U4 | 40.5* | 12.8 | 0 | 3 | 40.79* | 1.0072 | | | |
| 1'x4' | (Ag) | U5 | 32.18* | 10.3 | 0 | 2 | 32.74* | 1.0174 | | | |

* = before spire lamp change; redo = remeasurement of I-V

Note: U1, U2 and U5 had 8 strips and hence the lower power.

## Table 14. Module Performance after Sequence B Tests.

| | | | Sequence B: | | | | | | | | | | | | | |
|---|---|---|---|---|---|---|---|---|---|---|---|---|---|---|---|---|
| | Type | Ser.# | 50 T/C Pmax (w) | 50 T/C P/P(b.l.) | 50 T/C Voc(1 klux) | 50 T/C dry Hipot | 50 T/C wet Hipot | redo 50 T/C Pmax (w) | redo 50 T/C P/P(b.l.) | redo 50 T/C Voc(1 klux) | redo 250T/C Pmax (w) | redo 250 T/C P/P(b.l.) | 10 H/F dry Hipot | 10 H/F wet Hipot | 10 H/F Pmax (w) | 10 H/F P/P(b.l.) |
| L-strip | (Ag) | 212 | 7.14* | 1.0071 | 1.46 | 0 | 1 | 7.24* | 1.021157 | 1.47 | 6.83 | 0.963329 | 0 | 6 | 6.99 | 0.9859 |
| L-strip | (Ag) | 214 | 7.12* | 1.0028 | 1.46 | 0 | 0 | 7.13* | 1.004225 | 1.48 | 6.84 | 0.96338 | 0 | 2 | 6.84 | 0.9634 |
| 1'x4' | (Al) | C2 | 33.42* | 0.9673 | | 0.5 | 3 | 32.78 | 0.94877 | | | | 3 | 5 | 33.83 | 0.9792 |
| 1'x4' | (Al) | C3 | 34.42* | 0.943 | | 0.5 | 2 | 34.33 | 0.940548 | | | | 5 | 6 | 34.93 | 0.957 |
| 1'x4' | (Ag) | U2 | 29.36* | 0.9407 | | 0 | 2 | 29.14 | 0.933675 | | | | 4 | 5 | 29.26 | 0.9375 |
| 1'x4' | (Ag) | U3 | 38.7* | 0.9469 | | 0 | 2 | 38 | 0.929777 | | | | 2 | 2 | 37.59 | 0.9197 |

* = before spire lamp change; redo = remeasurement of I-V

Note: The columns under dry and wet Hipot indicate leakage current in microamperes.

## Table 15. Module Performance after Sequence C Tests

**Sequence C:**

| | Type | Ser.# | 239hD.H. dry Hipot | 239hD.H. wet Hipot | 239hD.H. Pmax (w) | 239hD.H. P/P(b.l.) | 239hD.H. Voc(1 klux) | 384hD.H. dry Hipot | 384hD.H. wet Hipot | 384hD.H. Pmax (w) | 384hD.H. P/P(b.l.) | 144hD.H. dry Hipot | 144hD.H. wet Hipot | 144hD.H. Pmax (w) | 144hD.H. P/P(b.l.) | 1006hDH dry Hipot | 1006hDH wet Hipot | 1006hDH Pmax (w) | 1006hDH P/P(b.l.) |
|---|---|---|---|---|---|---|---|---|---|---|---|---|---|---|---|---|---|---|---|
| L-strip | (Ag) | 217 | 0 | 4 | 7.1* | 0.997191 | 1.49 | 0 | 1 | 6.89 | 0.967697 | | | | | 0.5 | 6 | 6.94 | 0.974719 |
| L-strip | (Ag) | 218 | | | | | | 0 | 1 | 6.86 | 0.963483 | | | | | 1 | 4 | 6.9 | 0.969101 |
| 1'x4' | (Al) | C4 | | | | | | | | | | 0 | 4 | 34.11 | 0.943047 | 12 | 85 | 34.26 | 0.947194 |
| 1'x4' | (Al) | C5 | | | | | | | | | | 0 | 4 | 34.55 | 0.931016 | 20 | 50 | 34.82 | 0.938292 |
| 1'x4' | (Ag) | U4 | | | | | | | | | | 0 | 3 | 37.49 | 0.925679 | 9 | 26 | 37.6 | 0.928395 |
| 1'x4' | (Ag) | U5 | | | | | | | | | | 0 | 2 | 29.75 | 0.924487 | 18 | 20 | 29.82 | 0.926663 |

* = before spire lamp change; 144 and 384 hr damp heat ended at only 65% RH; 1006 hr damp heat tripped 17.5 hrs before hi-potting

Note: The columns under dry and wet Hipot indicate leakage current in microamperes.

## Sequence C Tests

The results from these tests are shown in Table 15. Note that although all the modules give acceptable power output, the leakage current is higher for the strip-interconnected modules. Further investigations are in progress with slightly thicker layer of encapsulant.

## Heat Cycling Test

The "heat cycling" test is essentially an in-house thermal cycling test in which the temperature range for the thermal cycles is approximately 0-90 °C. Two types of modules were fabricated in similar fashion for the test: material obtained from the production machine which uses Al/ZnO back reflector and 2B devices which use Ag/ZnO back reflector. Table 16 summarizes the results of eight modules before and after 180 cycles. The change in efficiency of the three production modules, TA 172, 174, and 176, after the test is within 0.8% of the respective initial values. The corresponding change for the 2B modules, numbers 2B 3972, 3987, 4014, and 4016, is 2.3%. Though the degradation is slightly higher for the 2B samples, it is still within reasonable limits. Module 2B 4036 exhibits an anomalous drop of 8.1% in efficiency.

## Heat Test

The "heat" test is an in-house test in which the modules are kept at 90 °C for several hundred hours. The results of the production TA and 2B modules are summarized in Table 17. The table shows the initial and final values of $V_{oc}$, $J_{sc}$, FF, and efficiency and the degradation in efficiency after the test. All the modules survive this severe test. The 2B modules exhibit slightly higher degradation than the TA2 material. Efforts are under way to plug this small difference.

## Thermal Cycling Test

This is the conventional thermal cycling test as specified in IQT NREL/TR-213-3624. Two production TA and two 2B modules which had been subjected to 180 "heat cycles" were used for the test. The results after 220 cycles are summarized in Table 14.

The degradation in all cases is within 1.5% of their respective initial values. The modules, therefore, pass the Phase II thermal cycle test milestone. As discussed earlier and as shown in the Phase I Annual Report, the production modules pass all the milestones.

**Table 16. Summary of 90 °C Heat Test of TA2 and 2B Modules.**

| Module # | Hours | $V_{oc}$ (V) | $I_{sc}$ (A) | FF | Efficiency (%) | Degradation (%) |
|---|---|---|---|---|---|---|
| TA72 | 0 | 1.77 | 5.73 | 0.661 | 7.4 | |
| | 565 | 1.80 | 5.71 | 0.677 | 7.5 | +1.3 |
| TA67 | 0 | 1.76 | 5.72 | 0.655 | 7.3 | |
| | 468 | 1.79 | 5.61 | 0.644 | 7.3 | 0 |
| TA68 | 0 | 1.75 | 5.60 | 0.643 | 6.9 | |
| | 468 | 1.78 | 5.55 | 0.654 | 7.1 | +2.9 |
| TA70 | 0 | 1.77 | 5.51 | 0.670 | 7.2 | |
| | 468 | 1.81 | 5.55 | 0.672 | 7.4 | +2.8 |
| 2B4074 | 0 | 2.30 | 5.77 | 0.666 | 9.7 | |
| | 565 | 2.32 | 5.62 | 0.671 | 9.6 | -1.0 |
| 2B4075 | 0 | 2.30 | 5.73 | 0.655 | 9.5 | |
| | 565 | 2.32 | 5.64 | 0.632 | 9.1 | -4.2 |
| 2B4077 | 0 | 2.28 | 5.89 | 0.654 | 9.7 | |
| | 565 | 2.31 | 5.78 | 0.648 | 9.5 | -2.1 |

**Table 17. Summary of Thermal Cycling of the TA2 and 2B Modules after 220 Cycles.**

| Module | Status | $V_{oc}$ (V) | $I_{sc}$ (A) | FF | $P_{max}$ (W) | Efficiency (%) | Degradation in $P_{max}$ (%) |
|---|---|---|---|---|---|---|---|
| TA 172 | Initial | 1.80 | 5.60 | 0.652 | 6.58 | 7.2 | |
| | Final | 1.78 | 5.50 | 0.663 | 6.50 | 7.2 | -1.2 |
| TA 174 | Initial | 1.78 | 5.56 | 0.654 | 6.48 | 7.1 | |
| | Final | 1.80 | 5.56 | 0.652 | 6.52 | 7.2 | +0.6 |
| 2B 4014 | Initial | 2.34 | 5.86 | 0.651 | 8.91 | 9.8 | |
| | Final | 2.30 | 5.79 | 0.657 | 8.77 | 9.6 | -1.5 |
| 2B 4016 | Initial | 2.34 | 5.82 | 0.664 | 9.06 | 10.0 | |
| | Final | 2.33 | 5.78 | 0.664 | 8.95 | 9.8 | -1.2 |

# Section 7

# Future Directions

We have completed the three-year research program and met many of the major milestones. This has been accomplished by optimizing the back reflectors, the component cells, the top conductive oxide, and the triple-junction structures. Uniformity over a one-square-foot area is essential in achieving high efficiency modules. We have overcome challenges encountered during the course of the work; we have also identified issues associated with fabricating even higher efficiency modules. The result of this research program, including back reflectors and the top cell, has contributed significantly to the achievement of a world record 13% stable active-area cell efficiency using the triple-junction approach. Utilizing the know-how and technology developed in this program, we shall continue to focus on remaining issues and further develop high stable efficiency modules at a lower manufacturing cost.

# REPORT DOCUMENTATION PAGE

*Form Approved*
*OMB NO. 0704-0188*



| 1. AGENCY USE ONLY (Leave blank) | 2. REPORT DATE | 3. REPORT TYPE AND DATES COVERED |
|---|---|---|
| | May 1998 | Final Technical Progress Report; 2 February 1995 – 28 February 1998 |

**4. TITLE AND SUBTITLE**
Thin-Film Amorphous Silicon Alloy Research Partnership, Final Technical Progress Report, 2 February 1995 – 28 February 1998

**5. FUNDING NUMBERS**
C: ZAF-5-14142-01
TA: PV804401

**6. AUTHOR(S)**
S. Guha

**7. PERFORMING ORGANIZATION NAME(S) AND ADDRESS(ES)**
United Solar Systems Corp.
1100 West Maple Road
Troy, MI 48084

**8. PERFORMING ORGANIZATION REPORT NUMBER**

**9. SPONSORING/MONITORING AGENCY NAME(S) AND ADDRESS(ES)**
National Renewable Energy Laboratory
1617 Cole Blvd.
Golden, CO 80401-3393

**10. SPONSORING/MONITORING AGENCY REPORT NUMBER**
SR-520-24723

**11. SUPPLEMENTARY NOTES**
NREL Technical Monitor: K. Zweibel

**12a. DISTRIBUTION/AVAILABILITY STATEMENT**
National Technical Information Service
U.S. Department of Commerce
5285 Port Royal Road
Springfield, VA 22161

**12b. DISTRIBUTION CODE**

**13. ABSTRACT** *(Maximum 200 words)*

This report describes the status and accomplishments of work performed by United Solar Systems Corp. under this subcontract. Investigations were carried out on Ag/ZnO, Ag/$TiO_2$/ZnO and Ag/$MgF_2$/ZnO back reflectors to assess their suitability for use in cell structures. Arrays of high-efficiency component cells were made over 1-$ft^2$ areas. Single-junction top cells were made with an average stabilized power density of 5.4 mW/$cm^2$ measured under global AM1.5 illumination. Single-junction middle cells were optimized to give average stabilized power density of 3.6 mW/$cm^2$ under global AM1.5 illumination with a cut-on filter with $\lambda > 530$ nm. Arrays of high-efficiency triple-junction cells of 0.25-$cm^2$ active area were fabricated over 1-$ft^2$ area with average stabilized efficiency of 12% as measured under AM1.5 illumination. A triple-junction module of a 416-$cm^2$ aperture area was fabricated with an initial efficiency of 11.7% and stabilized efficiency of 10.24%. A 922-$cm^2$ aperture-area module exhibited an initial efficiency of 11.5%. The novel laser-drilling approach was used successfully to fabricate modules of 1-$ft^2$ area with shadow loss of approximately 1%. Using this laser-drilling approach, an initial total-area efficiency of 11.5% was achieved in a triple-cell structure of 12.6 $cm^2$ area. An initial total-area efficiency of 10.6% was achieved in a module of 300-$cm^2$ area. Reliability studies based on NREL's Interim Qualification Testing were carried out to confirm the suitability of the module encapsulation materials and processes.

**14. SUBJECT TERMS**
photovoltaics ; amorphous silicon alloy research ; thin films ; back reflectors ; amorphous silicon alloy component cells ; triple-junction cells and modules ; laser processed module ; reliability testing

**15. NUMBER OF PAGES**
69

**16. PRICE CODE**

| 17. SECURITY CLASSIFICATION OF REPORT | 18. SECURITY CLASSIFICATION OF THIS PAGE | 19. SECURITY CLASSIFICATION OF ABSTRACT | 20. LIMITATION OF ABSTRACT |
|---|---|---|---|
| Unclassified | Unclassified | Unclassified | UL |